공학박사학위논문

Spray Characteristics of a Pintle Injector with Geometric Parameters

핀틀 분사기의 형상 변수에 따른 분무 특성

2020년 8월

서울대학교 대학원

기계항공공학부

이수지

ABSTRACT

Spray Characteristics of a Pintle Injector with Geometric Parameters

Suji Lee
Department of Mechanical and Aerospace Engineering
The Graduate School
Seoul National University

Recently, as interest in low-cost reusable launch vehicles has increased with the micro-satellite market, soft-landing techniques have become important. A pintle injector can help realize this because it is capable of thrust control. After being devised by TRW, it has been developed and researched since the early 2000s. However, published literature and information are limited and still lacks in the design of the geometry. In particular, the pintle injector has many geometric parameters that affect its performance, so research on these is essential.

This study examined the relationship between main geometric parameters and spray characteristics. Since the spray characteristics of the pintle injector are closely related to the combustion efficiency, it was analyzed through cold test. First of all, internal flow passage design was carried out to evenly inject the fluids for small thruster with a thrust ratio of 5:1. Various geometry cases were designed to maintain the axial

concentricity of the drive part, and optimal geometry condition was derived through experiments and numerical analysis.

Afterwards, the effects of the gap distance (G), a factor related to the control of annular flow's orifice area, on the spray characteristics were investigated. When G decreased at the same throttling level, the spray angle decreased because the momentum of the annular flow became relatively large. When G was fixed, the spray angle was almost constant even though the throttling level was changed. Droplet diameter also had a proportional relationship with G. Through the relationship between SMD and Weber number (We) and momentum flux ratio (J), it was found that pintle injector has two main atomization mechanisms. At the pintle tip, when the radial and annular flows collided vertically, there was breakup of the liquid sheet due to the difference in momentum, and additional breakup due to the shear force at the interface of the two fluids. The experimental correlations for the spray angle and SMD were obtained, and through this, the control range of G to maintain a specific SMD in all thrust levels was derived.

Cold test was also performed on another important geometric factor, skip distance. As the skip distance increased, the spray angle and SMD had a proportional relationship. While annular flow moved along the pintle surface, the velocity decreased due to the interaction between friction and the ambient air. Due to this, the momentum loss rate increased and such a tendency appeared. Change rate in the spray

characteristics due to the skip distance became larger under the low thrust level, and showed the maximum change especially under the throttling level of 20%. In order to analyze these trends in more detail, numerical analysis of the axial direction velocity of the annular flow near the pintle surface was carried out. In all throttling levels, developed region with a similar velocity profile was observed after a potential core where the velocity remained constant from the orifice exit to a certain distance. In particular, it was found that the potential core region was the shortest and the velocity decay rate was the highest under the throttling level of 20%. As a result, the change rate of the spray angle and SMD seemed to be largest at the throttling level of 20%. Through the decay rate of velocity according to the skip distance, variation rates of the spray angle and SMD were obtained. Finally, from the design perspective, appropriate skip distance was proposed in consideration of the standard deviation between each throttling level.

From this study, databases on the important geometric parameters were obtained. These results are expected to help understand the relationship between the skip distance and spray characteristics. In addition, it can be used to design a thrust control system to improve the spray efficiency as a reference for setting the orifice area control range of annular flow. In the future, the presented findings may provide guidance for the design of effective injectors to be used in throttleable engines.

***Keywords*:** Pintle Injector, Thrust Control, Geometric Parameters, Spray Characteristics, Annular Orifice Area, Gap Distance, Skip Distance

***Student Number*:** 2016-30188

LIST

CHAPTER 1

CHAPTER 2

CHAPTER 3

LIST OF FIGURES

LIST OF TABLES

NOMENCLATURE

Alphabet

A_{cyl}	Cylinder cross-sectional area
$A_{e,annular}$	Annular flow’s outlet area
$A_{e,radial}$	Radial flow’s outlet area
Ap	Angle parameter
BF	Blockage factor
C^*	Characteristic velocity
C_d	Flow coefficient
C_F	Thrust coefficient
D	Decay rate parameter
D_c	Combustion chamber diameter
D_o	Circumferential length of each hole
D_p	Pintle diameter
Dr	Decay rate
F	Rocket thrust
F_{2v}	Fourier filtering
G	Gap distance
$GCH4$	Gaseous methane
GOX	Gaseous oxygen
H	Outlet height
I	Intensity

J	Momentum flux ratio
K	Kinetic energy ratio
LOX	Liquid oxygen
l_{in}	Contraction length
L_s	Skip length
L_s/D_p	Skip distance
N_H	Number of total holes/slot
O/F	Oxygen to fuel mass flow rate ratio
P	Pintle number
P_c	Chamber pressure
PI	Patternation index
q	Relative flow intensity
r_1	Cylinder inner radius
r_2	Cylinder outer radius
Sp	SMD parameter
SMD	Sauter mean diameter
SUI	Spray uniformity index
TMR	Total momentum ratio
U	Velocity in axial direction
V	Velocity at orifice exit
We	Weber number

Greek

α	Spray angle
β	Contraction angle
ξ_{in}	Damping factor
ρ	Density
σ	Standard deviation

Subscripts

0	Value when skip distance is one
gas	Gas
liq	Liquid
m	Maximum

CHAPTER 1
INTRODUCTION

With the recent growth of the private space rocket market, price competitiveness has become an important requirement for commercial launch services. Consequently, interest in developing reusable launch vehicles has quickly increased in countries around the world. Planetary exploration for future energy sources has also attracted attention. Soft landing technology is a key factor in reusable launchers and extrasolar planet exploration. A throttleable rocket engine is an important technology that can help accomplish this mission, so extensive research is required.

There are several ways to control thrust, including changing the propellant's type or composition and adjusting the area of the nozzle throat or nozzle exit. However, these approaches are difficult to control due to physical limitations and high heat flux concentrated in the nozzle throat. In contrast, controlling the propellant mass flow rate is regarded as the simplest method. The relationship between rocket thrust and propellant flow rate is defined by Eq. (1):

$$F = \dot{m}V_e + A_e(P_e - P_a) \tag{1.1}$$

where F, $\dot{m}$, V_e, A_e, P_e, and P_a are rocket thrust, propellant mass flow rate, nozzle exit velocity, exit area, exit pressure, and free stream pressure, respectively.

There are various ways to adjust mass flow rate, such as controlling differential pressure or using a dual manifold, but the area control method is considered to be the most promising [1].

A pintle injector is a representative area control method. The pintle injector is capable of maintaining high performance during deep throttling process through a drive part that moves along the combustion chamber axis and flow control valve. Through this mechanism, TRW made it possible to optimize each function by separating the propellant injection function and the propellant flow control function as shown in Fig. 1.1. MIRA-150A, a TRW binary propellant rocket engine, also used this mechanism. The injector's moving part and the flow control valve were mechanically linked to fulfill the desired throttling level [2-6].

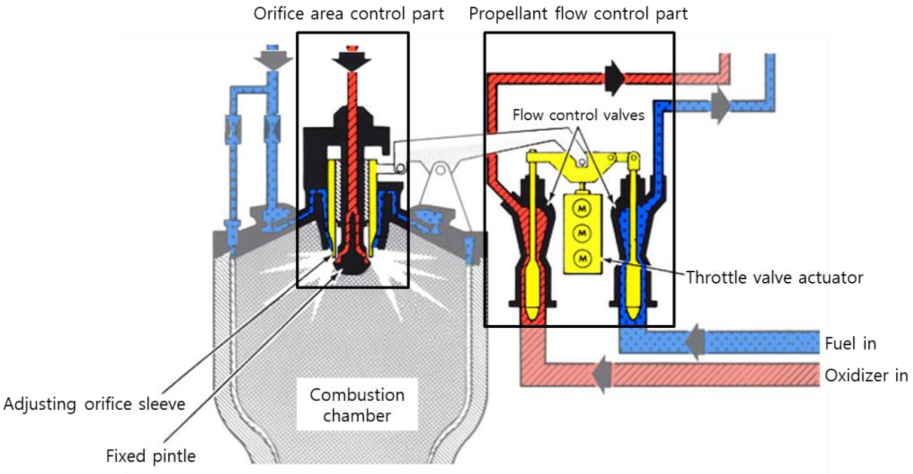

Fig. 1.1 Supply system diagram of Apollo lunar descent engine [6]

Compared to the fixed area type injectors, the thrust control method of the pintle injector has the following difference. In the case of the fixed area type, when the propellant mass flow rate is lowered by the flow control valve for thrust down, the velocity (V) and the pressure drop (ΔP) are decreased with the mass flow rate ($\dot{m}$) as shown in Eqs. (1.2) and (1.3). This may lead to poor spray efficiency and combustion stability, resulting in poor engine performance in low thrust level. On the other hand, the pintle injector can compensate for the decrease in V and ΔP by adjusting the orifice area (A) through the moving part. High spray efficiency and combustion stability can be achieved, thereby restoring the engine performance. Therefore, the pintle injector is effective for deep throttling.

$$\dot{m} = \rho V A \tag{1.2}$$

$$V = C_d \sqrt{\frac{2\Delta P}{\rho}} \tag{1.3}$$

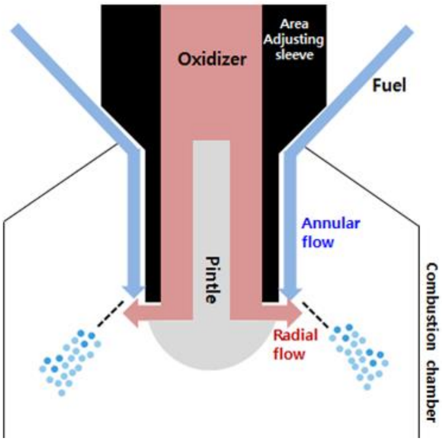

Fig. 1.2 Concept of pintle injector

In the Fig. 1.2, fuel is injected in the axial direction of the combustion chamber in the form of annular flow along the injector's outer wall. The oxidizer flows into the pintle injector and forms a thin sheet in the radial direction through the gap between the pintle and the sleeve. Propellants injected in the axial and radial directions collide with each other at the end of the pintle, allowing mixing and atomization to proceed.

This pintle injector has several characteristics. First, it can control the thrust and has consistent high performance over a wide thrust range. Second, only one pintle injector is required regardless of thrust, which can have a large range. For swirl or jet injectors typically used in liquid rocket engines, multiple injectors are mounted on one plate (Fig. 1.3). Consequently, cost and weight can be reduced because of this feature compared to conventional injectors. The third characteristic is combustion stability, as the pintle injector has recirculation zones around the injector. Because the recirculation zone at the center of the combustion chamber acts as a deflector and mixer for unburned droplets, it has a positive effect on combustion stability and performance [7, 8].

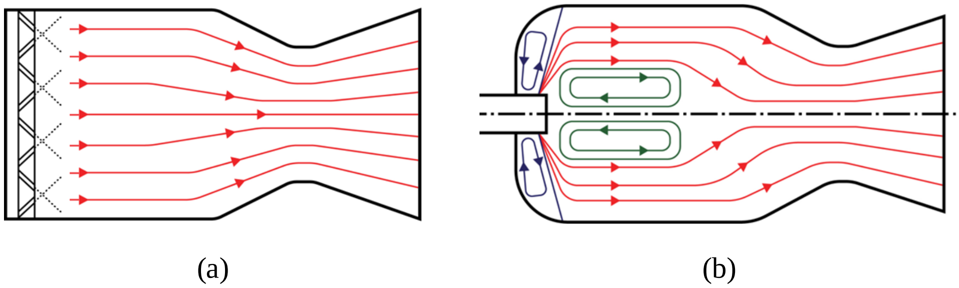
(a)
(b)

Fig. 1.3 Chamber flow patterns (a) typical liquid rocket (b) pintle rocket [7]

The pintle injector concept originated in Caltech's Jet Propulsion Laboratory in the mid-1950s, and it was applied to the Apollo lunar descent engine (LMDE) in the 1960s [9]. Since the early 2000s, pintle injector research has been carried out in industry and academia. SpaceX applied the pintle injector used in the LMDE to the Merlin engine to develop a reusable vehicle to reduce launch costs [10]. Northrop Grumman developed a TR202 prototype engine aimed at developing a variable thrust rocket engine for future NASA take-offs and landings. The combustion characteristics were observed through a 10:1 throttling level combustion test [11].

At Purdue University, a pintle injector for non-toxic bipropellants was developed and a combustion test was performed. Several parameters related to the pintle injector design were chosen to investigate how they affect combustion characteristics. In addition, as part of NASA's Morpheus project, a pintle injector for *LOX*/*LCH4* engine of a lunar lander was assembled and combustion tests were completed [12, 13]. At Minas Gerais Federal University in Brazil, various combinations were used to determine injection patterns of radial and annular flows, and the basic spray conditions of a prototype injector for a 1 kN engine [14]. In Germany, effects of pintle injector geometry on combustion and heat load were investigated. Four different pintle injector configurations were fabricated and evaluated for performance [15]. At the Indian Institute of Space Science and Technology, instability growth rate and droplet size were observed when radial and annular flows collided at different momentum ratios [16]. At the University of Tokyo, a combustion chamber applied a pintle injector, and the flame structure and combustion characteristics based on momentum ratios were identified [17, 18]. At China's National University of Defense Technology, a numerical analysis was performed to investigate effects of pintle injector geometry on the combustion chamber's internal combustion field. Specifically, combustion characteristics based on characteristic length, pintle opening distance, and pintle length were observed [19]. In Korea, at Chungnam National University, spray patterns and combustion performance were observed for various canted slit type pintle injectors [20-22]. Finally, at Korea Aerospace University, spray characteristics under various conditions were analyzed. In addition, recirculation zone and spray breakup simulations were carried out using a Lagrangian approach to numerical analysis [23-25].

Although some recent research has been conducted on pintle injectors many questions and limitations remain. The pintle injector has several geometric parameters that affect performance. However, compared to conventional injectors used in liquid rocket engines, there is very little research on the effects of theses parameters and little core information accessible within the published literature. In particular, there is a lack of research on the relationship between the geometric parameters and spray characteristics. Because the atomization efficiency of a pintle injector is related to the combustion characteristics and affects combustion performance [26], it is essential to analyze the spray characteristics. Therefore, more researches are required to improve the efficiency of the pintle injector.

In this study, the effects of geometric parameters on spray characteristics were analyzed for a 400 N class small thruster to obtain databases for optimal pintle injector design. In Chapter 2, a new design was performed to improve the uniformity of radial and annular flows of liquid/gas pintle injector. Experimental methods used to figure out the effects of geometric parameters were introduced in Chapter 3. In Chapter 4, the primary focus was the optimal orifice area control range of the annular flow. For this, a gap distance was changed, and the correlation with the spray characteristics was investigated. In Chapter 5, a skip distance associated with the moving distance of the annular flow along the pintle surface was focused. Spray characteristics were observed with the change of the skip distance.

CHAPTER 2
DESIGN OF PINTLE INJECTOR

2.1 Specifications and Basic Parameters

Table 2.1 Specifications of a 400 N thruster

Chamber Pressure (MPa)	1
Vacuum Thrust (N)	400
O/F	3.44
Chamber Diameter (mm)	54
Throttling Level (%)	20 to 100
Mass Flow Rate of Liquid Oxygen (g/s)	83.4
Mass Flow Rate of Methane (g/s)	24.24

The target engine of the pintle injector is a 400 N class small thruster that uses *LOX* and *GCH4*. Table 2.1 shows the specifications. The oxygen to fuel mass flow rate ratio (O/F) was set to 3.44, which is typical for a methane engine. Radial flow and annular flow were set as liquid oxygen and gaseous methane, respectively. The chamber diameter was calculated using Eq. (2.1), related to engine performance factors:

$$D_c = \sqrt{\frac{4}{\pi} \frac{F}{q\, C^*\, C_F\, P_c}} \tag{2.1}$$

where D_c, q, C^*, C_F, and P_c are combustion chamber diameter, relative flow intensity, characteristic velocity, thrust coefficient, and combustion chamber pressure, respectively. C^* (associated with combustion efficiency) and C_F (associated with nozzle efficiency) were obtained using NASA CEA code [27]. The throttling level was set to 20–100%, to achieve 5:1 deep throttling.

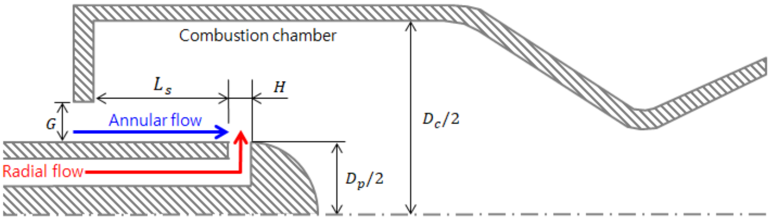

Fig. 2.1 Combustor of the pintle injector [28]

Fig. 2.1 shows several parameters that can determine pintle injector geometry; there were three main design factors, with the first being the ratio of chamber to pintle diameters (D_c/D_p). The diameter of the pintle injector was set at 11 mm, based on the recommended ratio of diameters 3 to 5 [28]. The second factor was skip distance, defined as the ratio of distance (until the annular flow first collides with the radial flow) to pintle diameter (L_s/D_p); its recommended value is 1. Previous numerical results showed that combustion efficiency decreased when skip distance was greater or less than 1. When the skip distance equaled 1, combustion efficiency was the highest [19]. Therefore, the default skip distance was set to 1, and L_s was determined to be 11 mm to the pintle diameter. The third parameter was the blockage factor (BF), defined as the ratio of the circumferential length of the holes or slot at the end of the pintle to the pintle circumference. BF is presented using Eq. (2.2), and the meaning of each parameter is shown in Fig. 2.2 [28, 29].

$$BF = (N_H D_o)/\pi D_p \tag{2.2}$$

where N_H and D_o are number of total holes/slot and circumferential length of each hole, respectively.

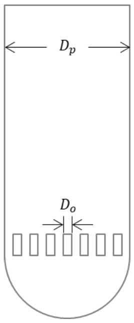

Fig. 2.2 Multi-hole type pintle geometry [29]

When BF was less than 1 (i.e., the circumferential length of the holes is smaller than pintle circumference) there were regions where annular and radial flow did not collide. This causes a reduction in mixing efficiency. In the previous study, it was confirmed that when the rectangular holes or canted slit were arranged at the pintle tip, the annular flow which did not collide with radial flow straightened in the axial direction of the combustion chamber. Also, as BF became smaller, the characteristic velocity efficiency decreased. This may be due to the reduced mixing area of the propellant, resulting in decreased mixing efficiency [20, 31, 32]. Therefore, the shape of the pintle injector associated with BF was focused on.

The pintle geometry known to date can be divided into two types as shown in Fig. 2.3. Figure 2.3 (a) and (b) differ in the injection method of the radial flow flowing into the pintle injector. Fig. 2.3 (a) is called the continuous slit type. This type has a structure in which the inner pintle flow path and the pintle outer wall are independently separated. Therefore, as in section A-A, the radial flow is ideally uniformly sprayed on all circumferences of the pintle and forms a thin liquid sheet. In this case, since BF is 1, all the propellants participate in the mixing. This has the most uniform spray pattern, but spray asymmetry can occur due to mechanical errors. The main reason for this was the maintenance of concentricity of the pintle rod. As the pintle rod moved up and down, the orifice size of the pintle was adjusted. In the case of this geometry, the pintle rod is mounted inside the passage of the radial flow, so the radial flow may have affected concentric maintenance. In addition, if such a concentricity maintenance problem occurs, it will adversely affect the radial flow so that it does not spray evenly on the circumference of the pintle.

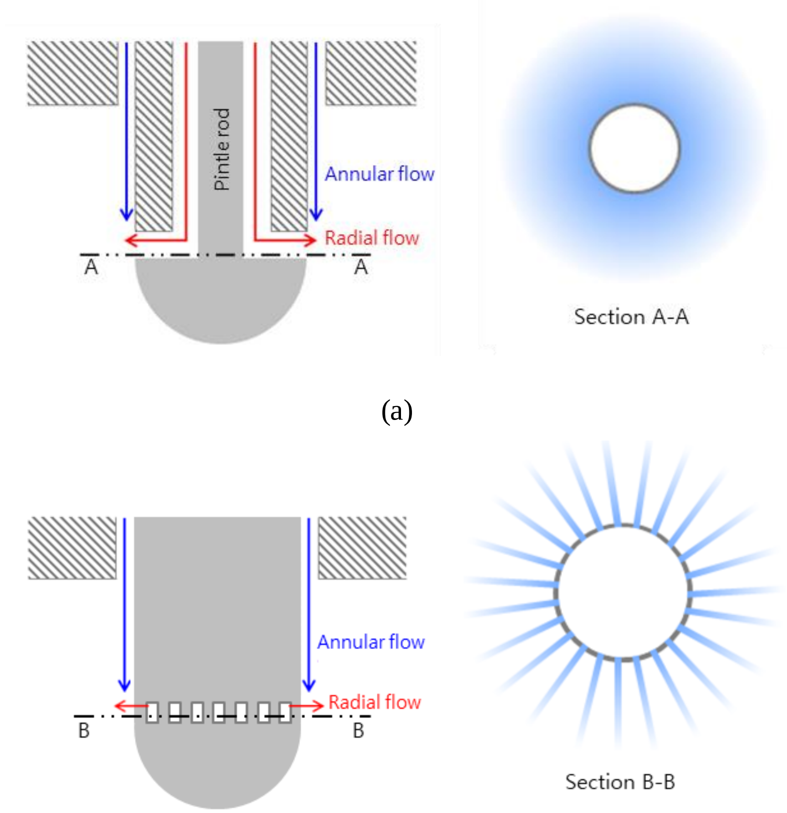

(a)

(b)

Fig. 2.3 Two types of pintle injectors (a) continuous slit type and (b) multi-hole type

The second type is the multi-hole type shown in Fig. 2.3 (b). This was mentioned earlier when BF was explained. The holes are arranged at the end of the pintle, and the radial flow is injected into the combustion chamber through these holes. The spray pattern of radial flow is like jet spray as shown in section B-B. This type has the advantage for adjusting the area of the orifice size. However, since BF is less than one, the spray quality is impaired. To solve this problem, the holes arranged in two rows or a canted slit was introduced. These geometries showed better mixing efficiency at fixed orifice size [22, 31]. But, this problem may occur again when the orifice area is reduced under low thrust conditions.

2.2 Design of Radial Flow Passage

To obtain a uniform spray pattern, a continuous slit type was adopted. To solve the main problem of this type, concentric maintenance, a new concept was applied. In the previous geometry, there was problem in which the radial flow and the pintle rod influenced each other. Therefore, a new design concept was devised to separate the radial flow passage and the pintle rod independently. To achieve this, a pintle injector with multiple inlet holes was designed. This is a structure in which the radial flow is supplied into the holes and spreads on whole circumference at the outlet. With this, it can separate the pintle rod so that the concentricity can be kept constant at all throttling levels.

Now the important thing was how to design the arrangement of the inlet holes and the flow path inside the pintle. In order to obtain the optimum geometry, three configurations of pintle injector with this concept were designed as shown in Fig. 2.4. In all three cases, the total area of the inlet holes was equal to 6.158 mm^2 using the discharge coefficient equation. Only the number of holes was different. The number of holes could be up to 8 due to manufacturing limit. Considering this, the number of holes of case 1 and case 2 were designed as 4 and 8 respectively, to identify the impact of the number of holes. Case 3 had 8 inlet holes, as in case 2, and there was cylinder passage after a specific length.

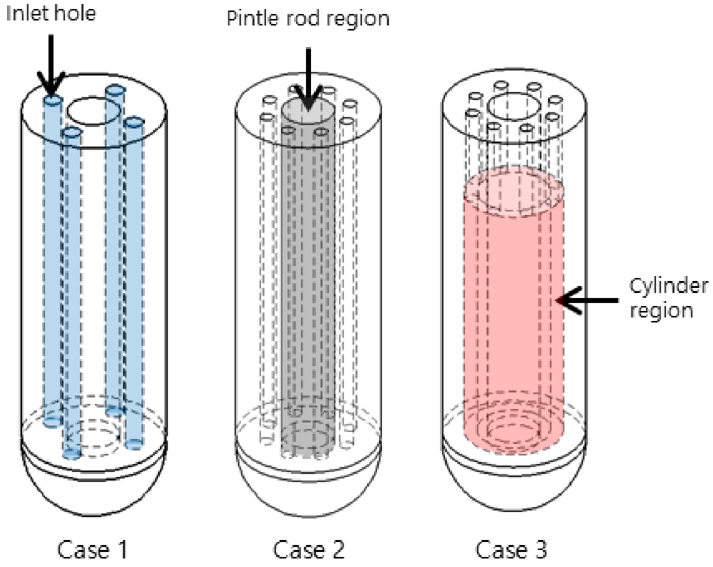

Fig. 2.4 Three configurations for radial flow passage

The front shape of the inlet hole was considered to minimize the pressure drop. Yang et al. [33] defined ξ_{in} as a damping factor related to the pressure drop, which is expressed by the ratio of the contraction angle (β) and the contraction length (l_{in}) in Fig. 2.5. The point where ξ_{in} became the minimum was 50° and 0.84 mm for β and l_{in}, respectively. However, in the case of β, it was designed at 45° in consideration of manufacturing processability.

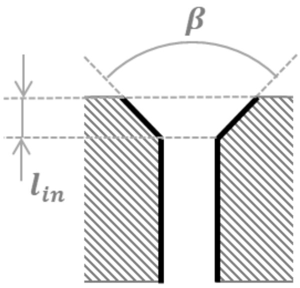

Fig. 2.5 Shape of contraction inlet hole

To check the uniformity of the radial flow for each configuration, spray tests were performed at 100% throttling level condition. Fig. 2.6 shows the spray patterns for each injector case. As considered during the design step, the radial flow spread in all directions. So, BF achieved 1 for all types. However, in case 1 and case 2, concentrated flow was observed between the holes. In the case 1, there were 4 holes, so 4 concentrated flows were observed. In the case 2, more concentrated flows were observed than in case 1. When the concentrated flows occurred, the momentum was relatively strong in the region. They did not form a specific spray angle after collision with the annular flow and were scattered to the side. In case of 8 holes, the amount of scattered droplets was lower than in the case of 4 holes. This was because, when the number of holes was increased under the same mass flow rate condition, the amount of superimposed fluid between the holes was reduced. Therefore, it was confirmed that a higher number of holes could be used to suppress the superimposed flow rate.

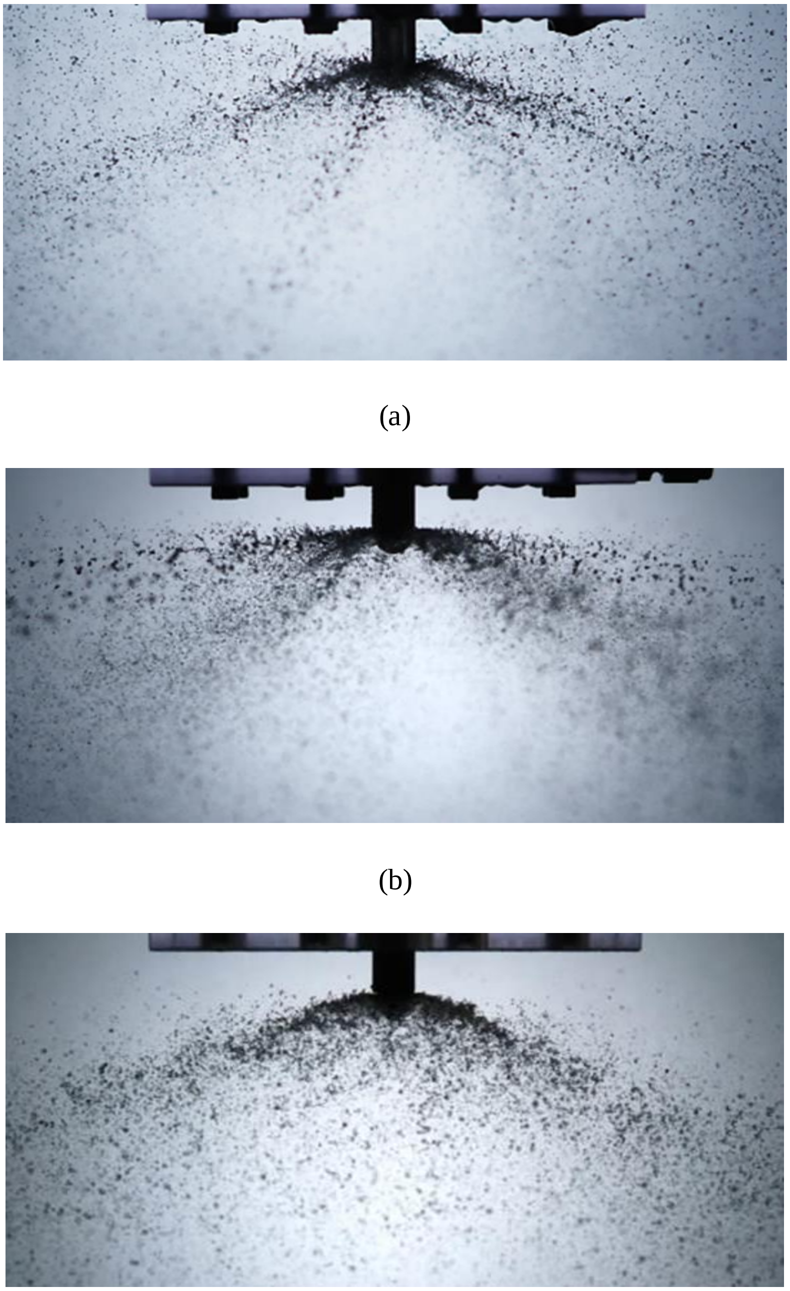

(a)

(b)

(c)

Fig. 2.6 Spray patterns of each case (a) case 1, (b) case 2, and (c) case 3

Since the number of holes was limited in production, the maximum number was 8, and then case 2 and case 3 were compared. High uniformity was observed in the case 3 under the same flow rate and number of holes. Unlike case 1 and 2, case 3 converged at a specific spray angle without the concentrated flow. Since the radial flows passing through each hole were mixed in the cylinder region before exiting the pintle outlet, a uniform distribution was formed.

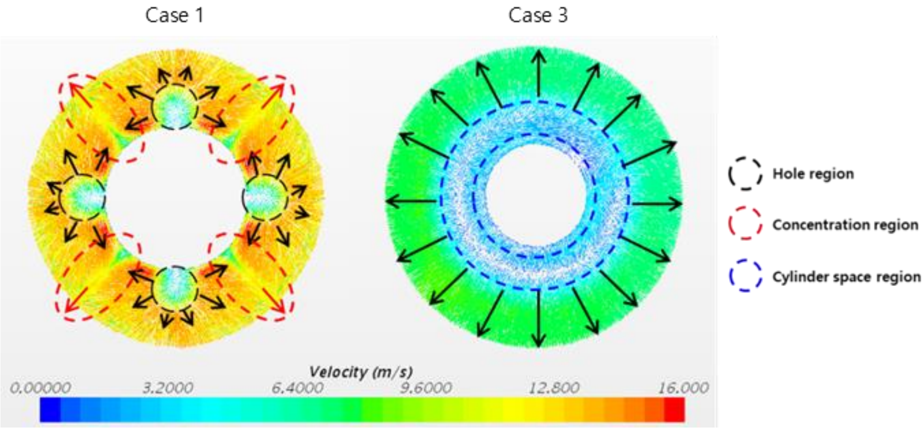

Fig. 2.7 Radial flow patterns at pintle outlet section

To observe these spray patterns in detail, numerical analysis was carried out only for the radial flow at the pintle outlet section. A commercial code STAR-CCM+ developed by SIEMENS was used for this. The geometry was three dimensional domain of the pintle outlet region. The boundary conditions of inlet and outlet were mass flow rate and atmospheric condition, respectively. Turbulence model was k-epsilon model. Internal flow pattern results at outlet section were like Fig. 2.7. In the case 1, the fluid exiting the hole spread out in all directions, and it was superimposed on the fluid flowing out of the other hole. This was consistent with the experimental result. On the contrary, in the case 3, it was shown that the spray had a uniform velocity field at the outlet. Thus, the case 3 was selected as the final geometry.

The detailed description of the case 3 geometry is as follows. To support the concentricity of the pintle rod, a guide wall was enclosed around the pintle rod, shown as red hatched lines in Fig. 2.8. This guide wall holds the pintle rod such that it does not wobble inside the pintle. As previously mentioned, this guide wall also eliminates the effects of the flow inside the pintle by independently separating the pintle rod from the inner passage of the radial flow.

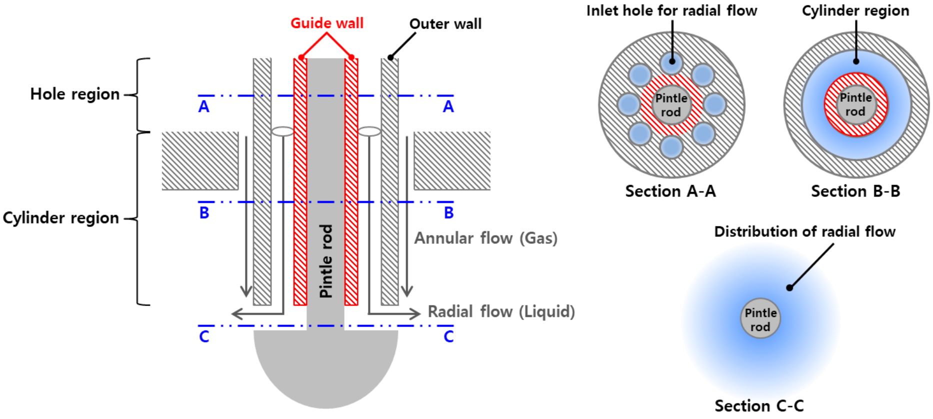

Fig. 2.8 New concept for maintaining concentricity of a pintle rod (case 3)

In the hole region, the areas between the holes serve to connect and support the guide wall with the outer wall. The radial flow is initially supplied into the multiple inlet holes, as shown in section A-A. It then passes through a cylinder region, as shown in section B-B in Fig. 2.8, for mixing of the fluids passing through each inlet hole. The cylinder region was placed before exiting the pintle outlet to form a uniform distribution. After passing through the cylinder region, the radial flow is distributed over the entire circumference of the pintle as shown in section C-C.

2.3 Design of Annular Flow Passage

Fig. 2.9 (a) shows the final geometry of the pintle injector. It consisted of a pintle post (the core of the pintle injector, with inner geometry as shown in Fig. 2.8), three manifolds to uniformly supply flows, pintle rod, and a micrometer head (Mitutoyo MHN1-25MXN, resolution 0.001 mm) to adjust the radial flow's orifice size. If the geometry changed, each corresponding part could be independently replaced.

As with the radial flow, it was important to obtain a uniform pattern of the annular flow. In particular, since the annular flow was supplied to one port located on the side as in Fig. 2.9, manifold design was important to have even distribution at the outlet. The parts related to this were the middle and down manifolds. However, the geometry optimization of these two manifolds still had an imbalance at the outlet side.

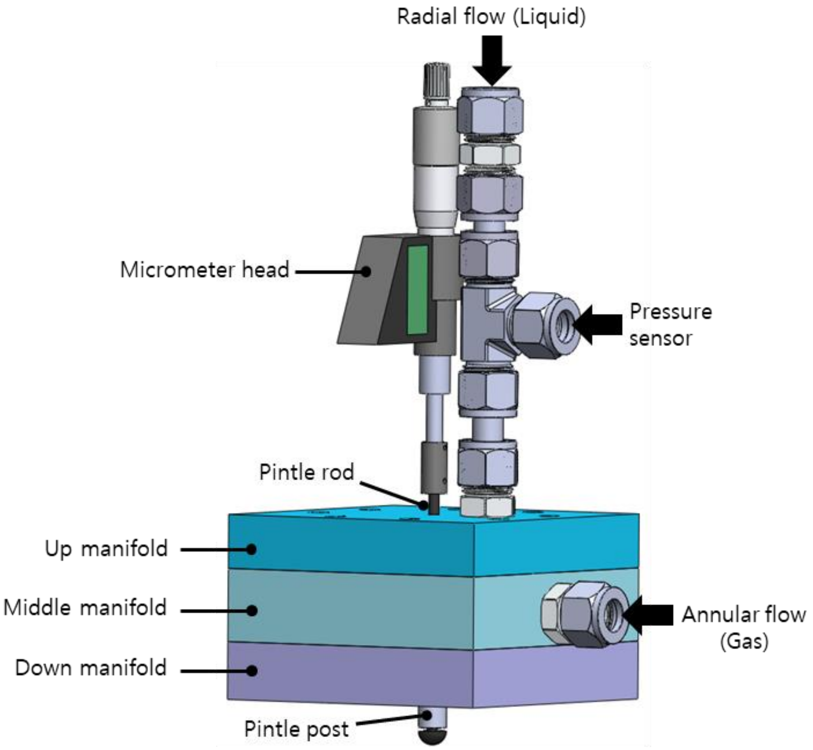

(a)

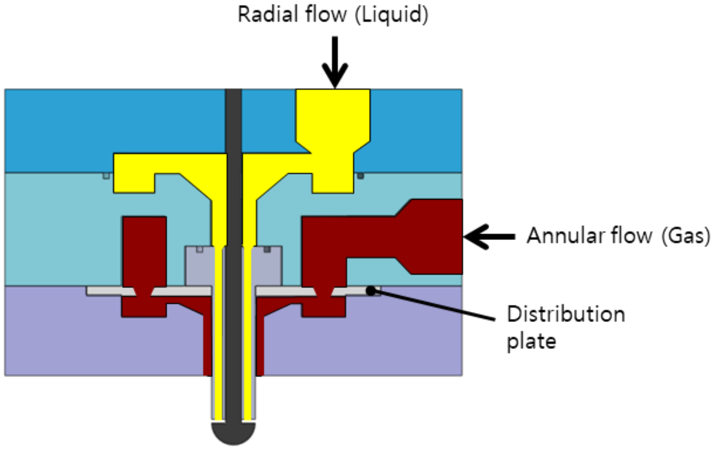

(b)

Fig. 2.9 Final geometry of the pintle injector (a) whole view and (b) section view

The method to resolve this problem was to insert a distribution plate between the two manifolds as shown in Fig. 2.9 (b). It was a thin Teflon plate with several holes, which helped to distribute the flow uniformly with the sealing effect. This type of plate was also used in previous study for uniform distribution of the propellant [14].

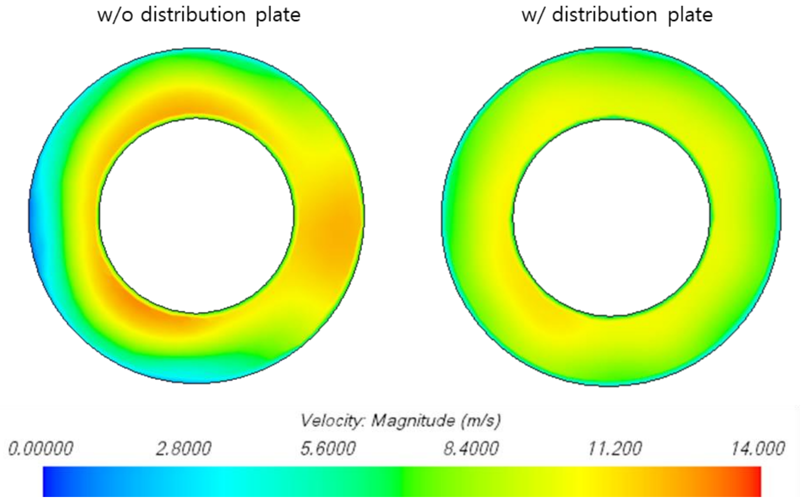

Fig. 2.10 Annular flow patterns at outlet section

Fig. 2.10 shows the magnitude distribution of the annular flow velocity at the outlet section with and without the distribution plate at throttling level of 20%. The code and boundary conditions were the same as those used for radial flow pattern analysis. Without the distribution plate, the annular flow inlet port side showed higher velocity region. The average velocity difference between left and right in the center line was about 40.89%. On the contrary, if there was the distribution plate, it could be seen that the outlet had a uniform distribution regardless of the location of inlet port. In this case, the average velocity difference was about 0.37%.

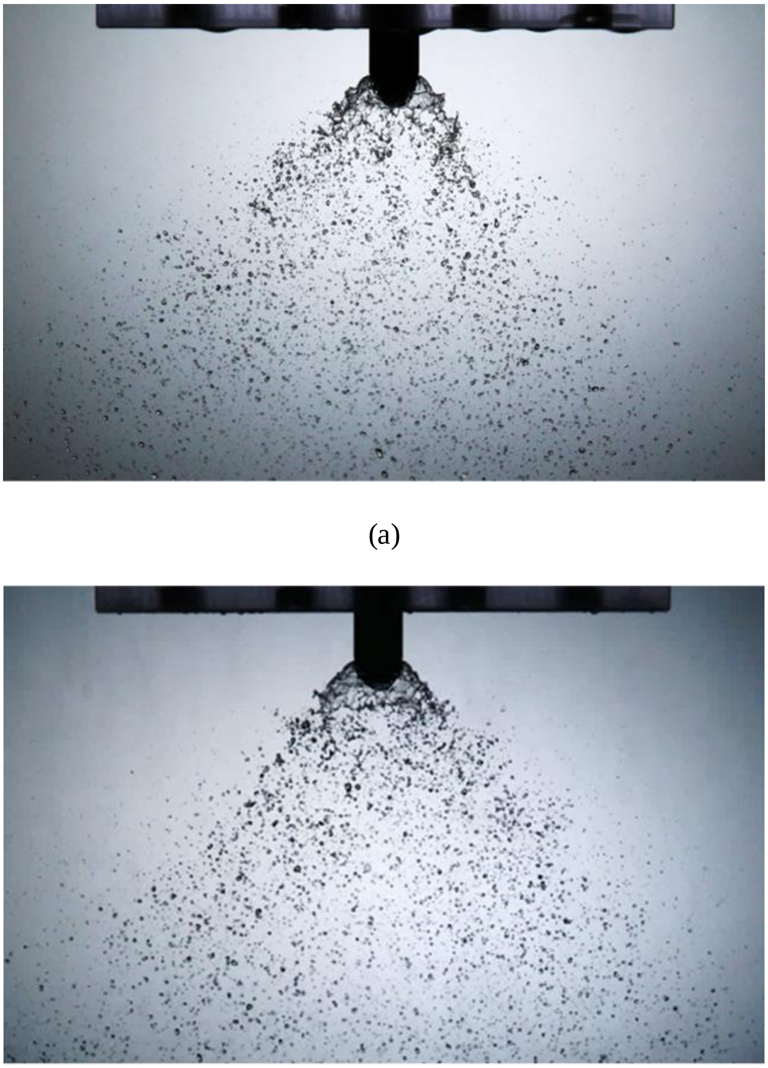

(a)

(b)

Fig. 2.11 Spray patterns (a) w/o distribution plate and (b) w/ distribution plate

The experimentally obtained spray patterns with and without distribution plate are shown in Fig. 2.11. This was done at throttling level of 20% and the difference between the two cases was clearly visible. When there was no distribution plate, the gas velocity in the region close to the inlet port was large, so the right spray angle was narrower compared to the left. Table 2.2 shows the spray angle errors between left and right compared to the right spray angle for both cases. Finally, in the subsequent experiments, the geometry in Fig. 2.9 with the distribution plate was used.

Table 2.2 Index of uniformity

Case	Half of Spray Angle		Error (%)
	Left	Right	
Fig. 2.11 (a)	39.7	25.5	55.69
Fig. 2.11 (b)	34.4	36	4.44

CHAPTER 3
EXPERIMENTAL METHODS AND SETUPS

3.1 Spray Imaging

Backlight photography was used to obtain the overall spray image. As shown in Fig. 3.1, this is a technique in which a light source and a digital camera face each other and the pintle injector is placed in the middle. It has the advantage that the shape of the spray can be made more prominent with backlight. In this study, stroboscope (SUGAWARA MS-230DA model) with a flash duration of 6 μs was used as the backlight. To acquire spray images, a digital camera (Canon EOS 7D, 5184 x 3456 pixels, spatial resolution 47 μm/pixel) and a lens (Canon EF 24-70 mm) were used. The frozen image was obtained by setting the camera exposure time and the flash frequency of the stroboscope the same.

For the cold test, water and air were used as simulants for LOX and GCH4, respectively. There was a pressurized tank at the front of the feed line of each fluid, which was controlled to supply fluid to the injector’s manifold. Liquid supply line was equipped with mass flow meter (KOMETER KTM-800, accuracy ±0.5%) for mass flow rate monitoring and a needle valve as the flow control valve. Gas feed line was equipped with a mass flow controller (MKP TSC-150, accuracy ±0.2%) for flow control between the gas supply system and the manifold.

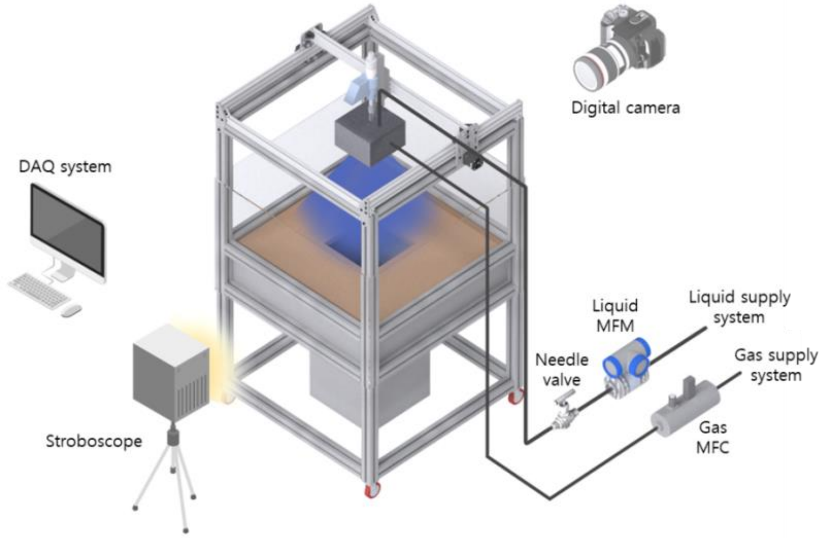

Fig. 3.1 Experimental setup for backlight photography

3.2 Droplet Size (SMD)

The droplet size is a key parameter related to spray performance and further affects combustion efficiency. To observe the droplet size, an experimental apparatus was set up as shown in Fig. 3.2. It consisted of CMOS high speed camera (Photron FASTCAM SA5, 1024 x 1024 pixels), a long distance microscope (LaVision QM1) with a magnification lens x2.0, and the stroboscope. The spatial resolution 4.59 $\mu\mathrm{m/pixel}$, and 200 images were taken per case. Droplet size was measured at a point 20 mm from the pintle tip in the axial direction to the outline of the spray field.

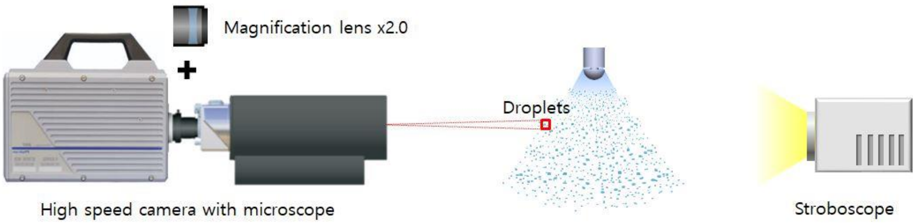

Fig. 3.2 Droplet size measurement setup

Fig. 3.3 shows the image processing procedure used to measure droplet size. The raw image taken by the camera was recorded in grayscale, and the optimal threshold was calculated based on Otsu's method. In the resulting binary image, droplets were clearly visible apart from the background. The spray image contained background errors such as dust on the detector. To eliminate these errors, a background image taken without spraying was also binarized and then subtracted from the spray image. In the last step, droplets in the image boundary were excluded. Non-circular droplets were removed based on the ratio of a minor axis length to a major axis length. This processing was performed for each image and the droplet size was obtained from a total of 200 images for each case.

To analyze droplet size, the Sauter mean diameter (SMD) was used. The SMD, also called D_{32}, is expressed in Eq. (3.1) as a ratio of volume to surface, and is a representative diameter that reflects evaporation rate and combustion reaction [34]:

$$SMD = \frac{\sum N_i \cdot D_i^3}{\sum N_i \cdot D_i^2} \tag{3.1}$$

where N_i and D_i are the number of droplets and the middle diameter in size range i, respectively.

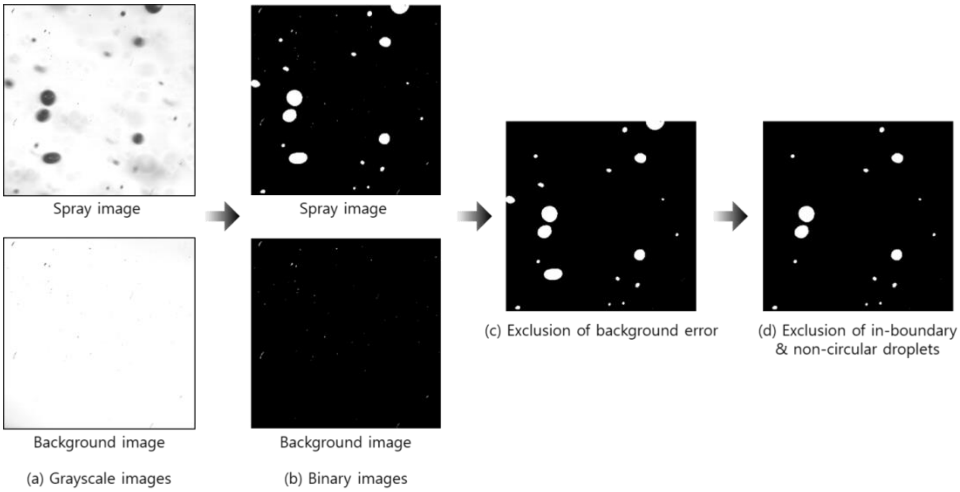

(a) Grayscale images (b) Binary images (c) Exclusion of background error (d) Exclusion of in-boundary & non-circular droplets

Fig. 3.3 Image processing for droplet size measurement

3.3 Spray Pattern

To analyze the degree of uniformity, the spray pattern perpendicular to the spray direction was measured using the optical patternator. This technique has a high spatial resolution and rapid characterization but can contain error sources such as multiple scattering and signal attenuation [35]. Therefore error corrections were applied.

The experimental setup consisted of a high speed dual head laser (Photonics Industries DM20-527DH) generating double pulses and a structured laser illumination planar imaging (SLIPI) module producing a two modulated laser sheets, and high speed camera with a lens (AF MICRO NIKKOR 105 mm) for detecting signals as shown in Fig. 3.4.

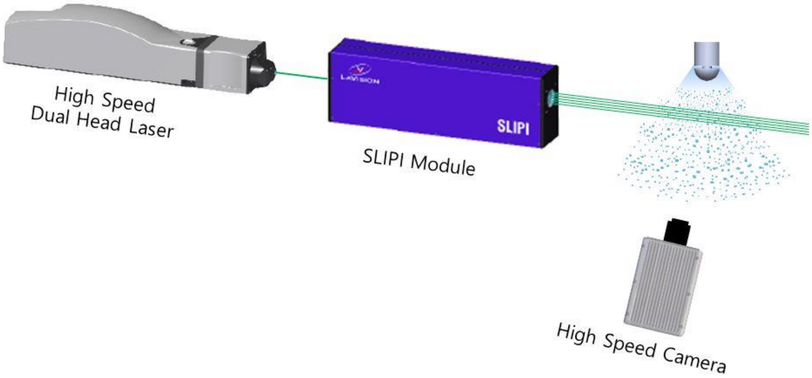

Fig. 3.4 Optical patternator setup

The camera was positioned perpendicular to the laser and was tilted upward because the spray cross section needs to be captured. In this position, a perspective error may occur, which means that the spray cross section appears to be skewed rather than the frontal view. To resolve this error, a calibration plate of LaVision was used to correct the tilted image. Because the original geometry information of this calibration plate was stored in LaVision's SprayMaster software, the degree of the error from the slanted plate image was identified through software post-processing. This calibration information was applied to the distorted spray image obtained from the actual spray test. In addition, when the camera was tilted, the lens plane was not parallel to the spray cross section plane. There is a problem that the focus was not formed in the entire field of view. In this case, the out-of–focused spray region has a blurring phenomenon and can’t obtain an accurate signal. This could be solved by inserting a Scheimpflug adapter between the camera and the lens. In general, the camera and the lens are fixed, but the angle of the lens can be changed independently by using this adapter. When the lens angle is adjusted so that the spray plane and the sensor image plane and the lens plane intersect at one point, called Scheimpflug intersection, a focus can be formed on the entire tilted spray image [36]. In this study, LaVision’s Scheimpflug adapter was used to obtain the lens angle at which the focus was formed on the whole area of the spray cross section plane. The camera was set to double frame to accept the double pulses from the laser, f/5.6, image rate of 3 kHz, and 300 images were obtained for each condition.

The structured laser illumination planar imaging (SLIPI) module is an optical device that eliminates multiple scattering in dense sprays. This uses a grating to illuminate a sinusoidal pattern on the laser sheet. So the modulated laser sheet is emitted at the outlet as shown in Fig. 3.4. This modulated laser sheet is responsible for distinguishing only a single scattering signal from unwanted signals. SLIPI is divided into three ways depending on the number of images required. In this study, a two phase SLIPI (2p-SLIPI) method was used to eliminate the multiple scattering. This makes the device configuration comparatively simple and well preserves the spatial resolution. It uses two modulated images with spatial phases of 0° and 180°, respectively. Then the 2p-SLIPI image is obtained by taking the absolute value of the intensity difference of the two images. In subtracting the two images, the multiple scattering is removed and then only single scattering signal is obtained. In this process, residual lines are visible at the point where the intensity difference is zero. This can be removed using Fourier post-processing. Finally, the light intensity of 2p-SLIPI image is given by Eq. (3.2) [37].

$$I_{2p-SLIPI} = F_{2\upsilon}\sqrt{(I_0 - I_{180})^2} \tag{3.2}$$

where $I_{2p-SLIPI}$, I_0 and I_{180} are intensities of the 2p-SLIPI image, phase 0° and 180° modulated images, respectively. $F_{2\upsilon}$ is Fourier filtering to reject the residual lines.

In this study, the average of 300 images for each condition was post-processed by using LaVision's SLIPI software and finally 2p-SLIPI image was obtained. The modulated laser sheet position was 7 mm from the end of the pintle rod in the axial direction, taking into consideration the diameter of the small combustion chamber and field of view.

To deal with signal attenuation, a compensation method proposed by Abu-Gharbieh et al. [38] was used. This method was based on the Beer-Lambert law and compensated for each pixel by applying a compensating algorithm in a discrete way. The detailed process was presented in a previous study [38].

CHAPTER 4

EFFECTS OF GAP DISTANCE ON SPRAY CHARACTERISTICS

4.1 Objectives

The key point of the pintle injector is that it adjusts the orifice area of the propellant during thrust control. In order to maintain high spray performance, the control of the orifice must be operated within appropriate range. Therefore, it was intended to provide database for finding the optimal control range of the annular (gas) orifice area. By changing the gap distance associated with gas orifice area, the spray characteristics were observed and the correlation between them was analyzed. At this time, the skip distance (L_s/D_p) was fixed to 1.

4.2 Experimental Conditions

Spray characteristics were observed at the minimum, mid-range, and maximum throttling levels of 20, 60, and 100%, respectively. In this study, throttling level was defined based on mass flow rates. Based on actual thrust, there may be a difference in throttling level due to changes in temperature, recirculation zone, pressure drop, flow coefficient, etc. To achieve a deep throttling of 5:1, the needle valve and the outlet height (H) related to the orifice area of the radial flow had to be adjusted simultaneously. Table 4.1 shows the operating range of H according to throttling levels as well as the corresponding mass flow rate. H was adjusted between 0.1 and 0.6 mm, a wide operation range that was accounted for when determining the minimum opening.

Table 4.1 Experimental conditions for gap distance

Throttling Level (%)	**20**	**60**	**100**
Liquid Mass Flow Rate (g/s)	16.6	49.67	83.58
Gas Mass Flow Rate (g/s)	1.98	5.92	9.95
Outlet Height (mm)	0.1	0.35	0.6
Gap Distance (mm)	0.234–3.95	0.503–3.95	0.986–3.95
Annular Orifice Area (mm^2)	8.26–185.52	18.18–185.52	37.13–185.52
Liquid Pressure Drop (MPa)	0.02	0.08	0.22
Gas Pressure Drop (MPa)	0.01–0.04	0.04–0.09	0.1–0.12

The maximum value of H was determined by considering the cylinder cross-sectional area (A_{cyl}) inside the pintle injector and the radial flow's outlet area ($A_{e,radial}$). These areas are expressed by Eq. (4.1), and each is shown in Fig. 4.1. If $A_{e,radial}$ was larger than A_{cyl}, the radial flow's orifice size was fixed to A_{cyl} even if H increased. In other words, the variation of the H was meaningless in this range. Therefore, the maximum adjustment value of H was set to

$$\left.\begin{aligned} A_{cyl} &= \pi(r_2^2 - r_1^2) \\ A_{e,radial} &= \pi D_p \cdot H \end{aligned}\right\} A_{e,radial} \le A_{cyl} \text{ @ } H \le 0.6\,mm \tag{4.1}$$

where r_1 and r_2 are cylinder inner radius and cylinder outer radius, respectively.

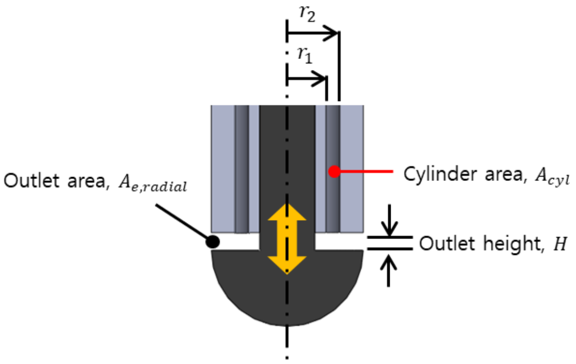

Fig. 4.1 Schematic of pintle tip

H was linearly controlled based on throttling levels. H values at throttling levels of 20, 60, and 100% were 0.1, 0.35, and 0.6 mm, respectively.

The gap distance (G) of the annular flow was an important parameter to be examined. It was a factor related to the orifice area of the annular flow (gas) as shown in Fig. 4.2. Spray characteristics were observed at each throttling level with various G. In Table 4.1, a specific G range was chosen for each throttling level to obtain accurate empirical correlations for spray angle and droplet size. The down manifold was manufactured for each G and then G was changed by replacing the down manifold as shown in Fig. 4.2. The adjustment range of the corresponding annular orifice area ($A_{e,annular}$) was obtained by Eq. (4.2).

$$A_{e,annular} = \pi G \cdot \left(D_p + G\right) \tag{4.2}$$

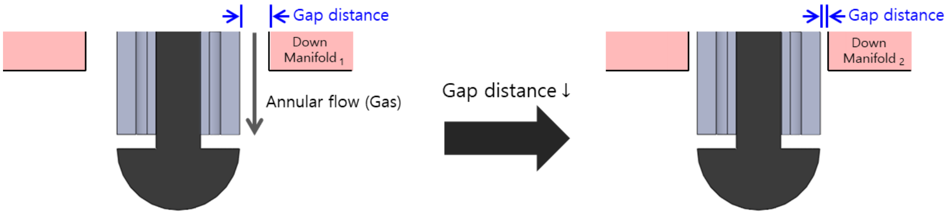

Fig. 4.2 Change of gap distance

The gas flow rate was adjusted such that water to air mass flow rate ratio was maintained at 8.4, regardless of thrust. It was for similarity of total momentum ratio (TMR) between simulants and real propellants in nominal pressure.

4.3 Results and Discussion

4.3.1 Spray Structure

Fig. 4.3 shows spray images for all experimental conditions. The breakup process was classified into two types: (type-A) droplets split from a liquid sheet after collision of the radial and annular flows and (type-B) atomization immediately after collision. The type-A was observed when the throttling level was 20% and G was greater than 1.835 mm. To set the criterion for dividing the two breakup mechanisms, momentum flux ratio (J) and Weber number (We) for two-phase flow defined as Eq. (4.3) and Eq. (4.4), respectively.

$$J = (\rho V^2)_{liq}/(\rho V^2)_{gas} \tag{4.3}$$

$$We = \{\rho_{gas}(V_{gas} - V_{liq})^2 H\}/\sigma_{liq} \tag{4.4}$$

where ρ_{gas}, ρ_{liq}, V_{gas}, V_{liq} and σ_{liq} are gas density, liquid density, gas velocity, liquid velocity, and liquid surface tension, respectively. The characteristic length of the pintle injector was defined as H.

Results confirmed that type-A occurred when J was greater than 38.1 and We was less than 0.52. In this region, there was a specific breakup length and droplet size was relatively large compared to type-B as shown in Fig. 4.4 (a). That is, atomization efficiency was relatively low, and accounting for the small thruster, combustion efficiency can be adversely affected. This again illustrated that annular flow orifice size control was important to optimum spray performance. To obtain optimum injector parameters, spray characteristics were therefore analyzed except for this region.

For type-B, the typical atomization process is shown in Fig. 4.4 (b). After the thin liquid sheet in the radial direction collided with the annular flow, a short-length wave was generated by aerodynamic force, leading to the disconnection of the liquid sheet. Furthermore, a liquid lump fell out of the end of the liquid sheet and then split into smaller droplets. This process took place immediately near the pintle tip.

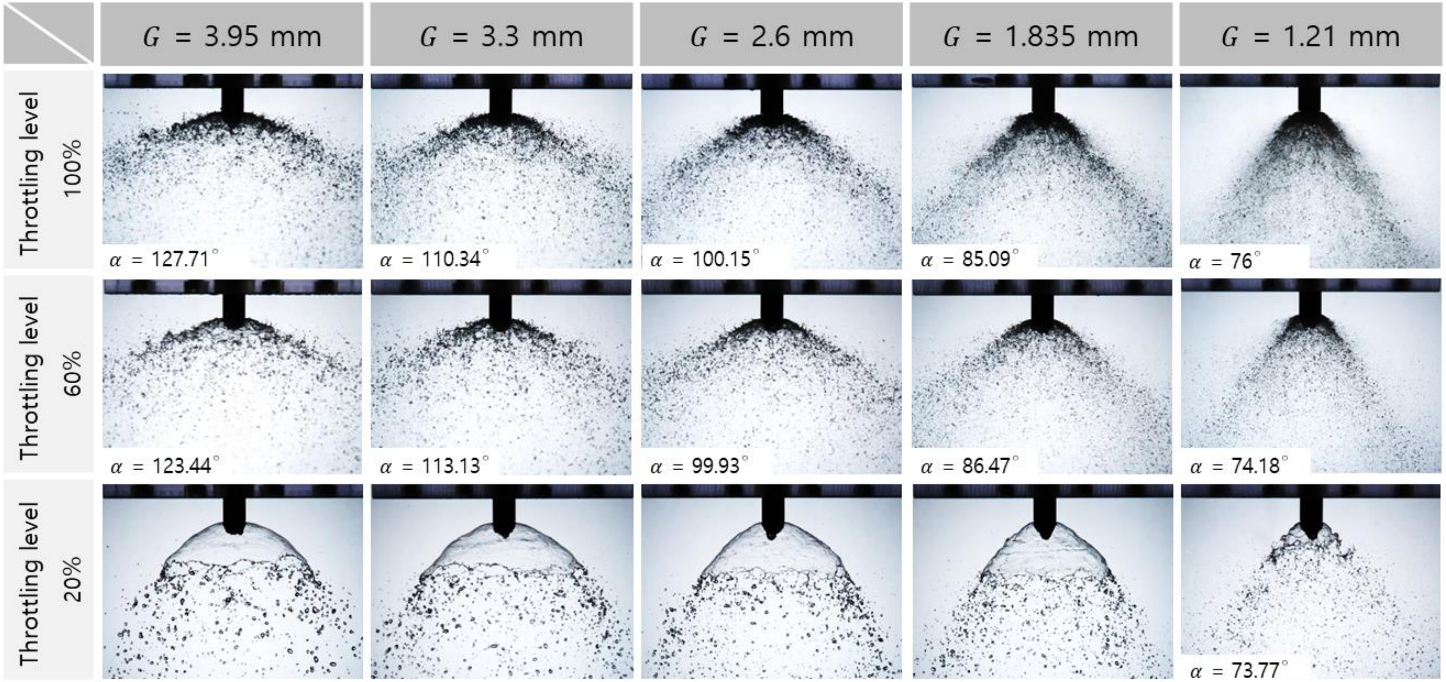

Fig. 4.3 Spray images with various throttling levels and gap distances (continued)

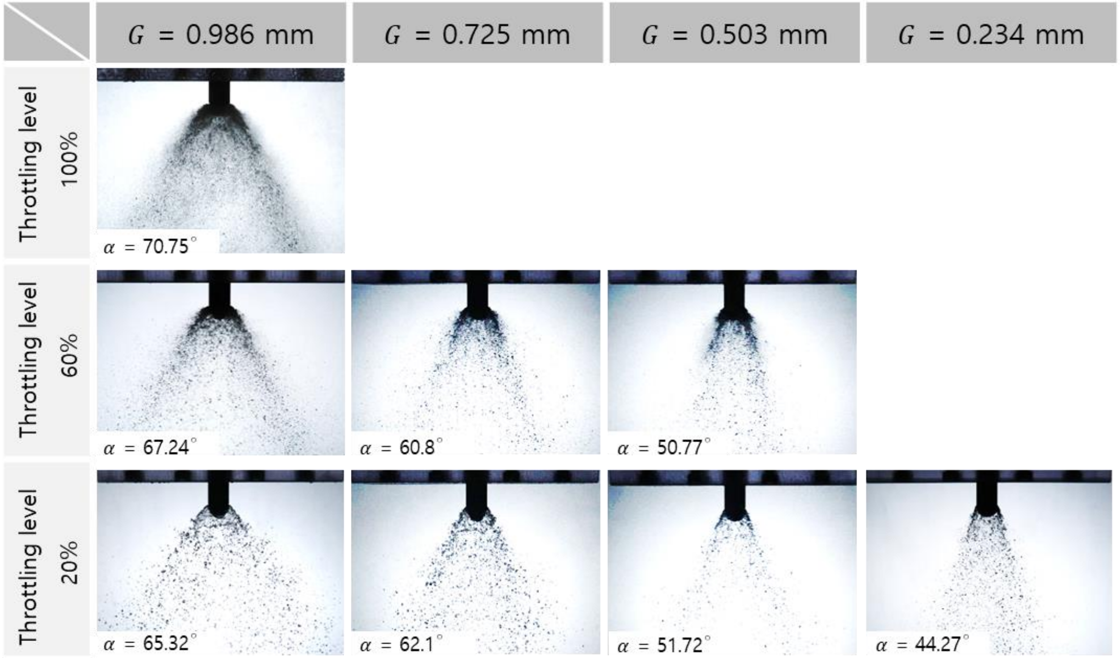

Fig. 4.3 Spray images with various throttling levels and gap distances

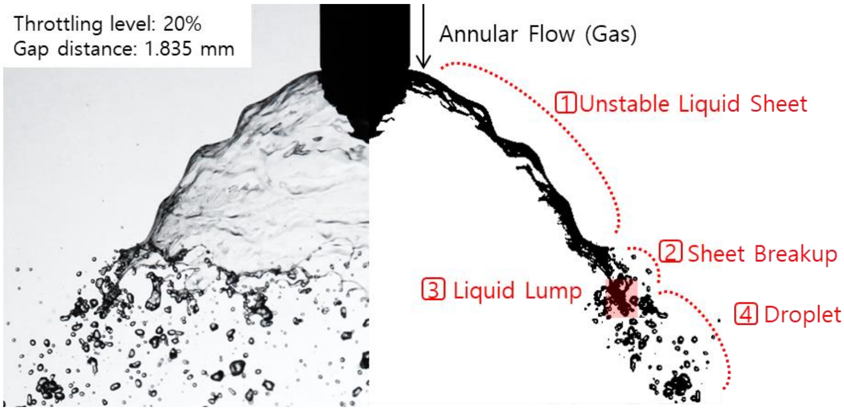

(a)

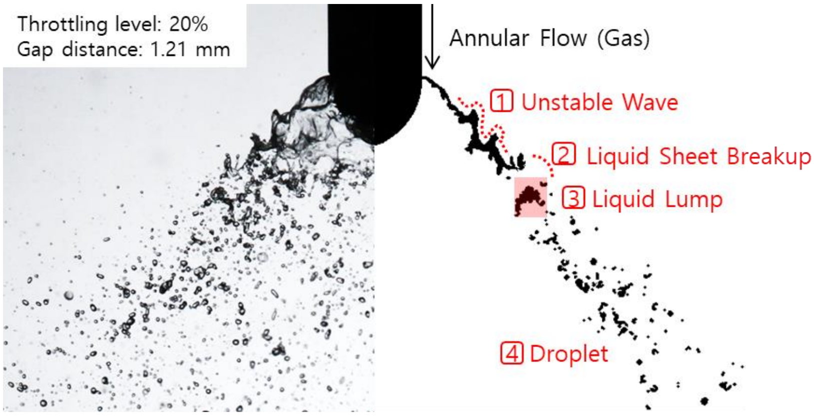

(b)

Fig. 4.4 Atomization process (a) type-A, G = 1.835 mm and (b) type-B, G = 1.21 mm

To obtain the spray angle, 50 images were averaged for each case. The spray angle decreased with decreasing G (Fig. 4.3), explained by total momentum ratio (TMR), which is closely related to the spray angle formation of the pintle injector [28, 29]. In previous study, correlation with the spray angle was investigated for TMR and J.

For this, liquid/gas pintle injector was used. As a result, TMR had a higher correlation with the spray angle. It seemed to be due to the consideration of the orifice area since TMR includes the mass flow rate unlike J [30].

TMR is defined in Eq. (4.5) and is expressed as the ratio of momentum of radial flow (liquid) to annular flow (gas).

$$TMR = (\dot{m}V)_{radial}/(\dot{m}V)_{annular} \tag{4.5}$$

At each throttling level, mass flow rates of liquid and gas were fixed. In addition, because H associated with the liquid orifice size was constant at each level, the liquid momentum was fixed. As G decreased, the gas orifice size also decreased while gas velocity increased. As a result, as G decreased, gas momentum intensified and spray angle decreased.

Fig. 4.5 (a) shows that spray angle was proportional to TMR. When G was the same, the spray angles at all throttling levels were nearly identical. From the perspective of TMR, it can be expressed as $TMR \propto f(H^{-1})$ under conditions where G is the same in the entire throttling range. In other words, points with the same spray angle had different TMRs. This is because H changes linearly with throttling level. Therefore, if the throttling level decreases under the same G condition, TMR increases.

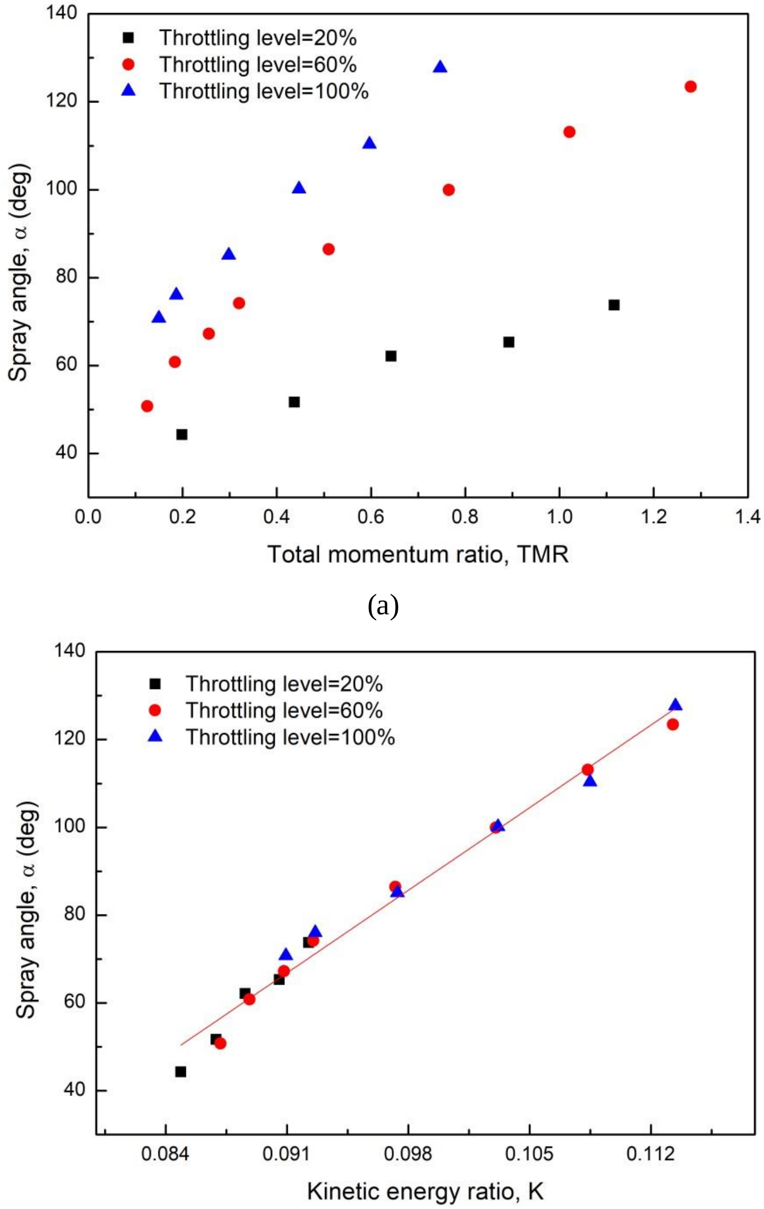

(a)

(b)

Fig. 4.5 Relationship between spray angle and (a) total momentum ratio, TMR

(b) kinetic energy ratio, $K = TMR\ (H/G)$

For this characteristic, there was a gap (Fig. 4.5 (a)) such that only the correlation between the spray angle and TMR was expressed. Therefore, a new dimensionless number was defined to represent spray angle tendency within the overall thrust range. Fig. 4.5 (b) shows spray angle tendency with a kinetic energy ratio (K), defined by Eq. (4.6), which is related to the ratio of H to G in TMR. It can be physically expressed as the ratio of the kinetic energy of the liquid and gas related to the spray formation of the liquid-gas injector. As K increased, the kinetic energy of the gas decreased, and thus the spray angle increased.

$$K = TMR\,(H/G) \tag{4.6}$$

For K, it can be expressed as $K \propto f(G)$. That is, if G is the same, the value of K is also constant irrespective of the throttling level. This allows the same spray angles to have one K and eliminates the gap that was observed between the throttling levels in TMR and spray angle relationships. As a result, it can be expressed as one correlation having a proportional relationship. The correlation between K and spray angle (Fig. 4.5 (b)) was defined as Eq. (4.7), with R^2 = 0.98. This empirical equation will be used to predict the spray angle in future spray conditions.

$$\alpha = 2687.78\,K - 177.74 \tag{4.7}$$

4.3.2 Droplet Size (SMD)

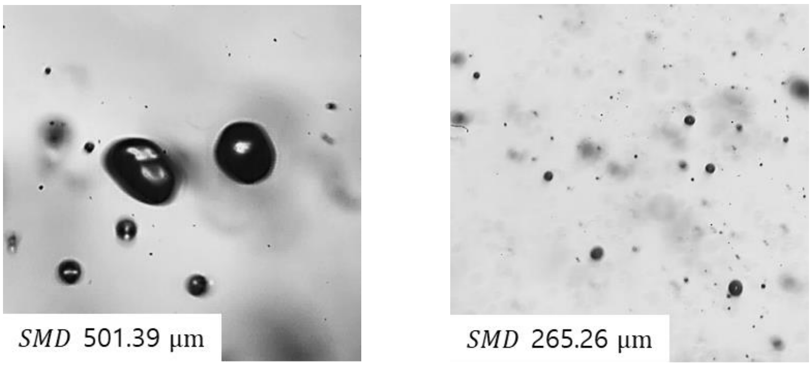

(a) (b)

Fig. 4.6 Droplet images at throttling level of 20% (a) G = 1.21 mm and (b) G = 0.234 mm

Fig. 4.6 shows an example of the trend of SMD according to G. As G decreased, atomization became more active. In order to increase the rocket's combustion efficiency, SMD must be kept below a certain level, and through this, it can be confirmed that the control of G is essential to achieve the target SMD under all thrust levels.

For SMD analysis, J and We were selected. Both are closely related to breakup, especially J has been used in the breakup mechanism of jet in crossflow. Fig. 4.7 shows SMD trend based on each dimensionless number, and indicates that both were related to SMD formation in the pintle injector. These results could be correlated with the pintle injector's breakup mechanisms. As shown in Fig. 4.8, the first breakup was a vertical collision like a jet in crossflow.

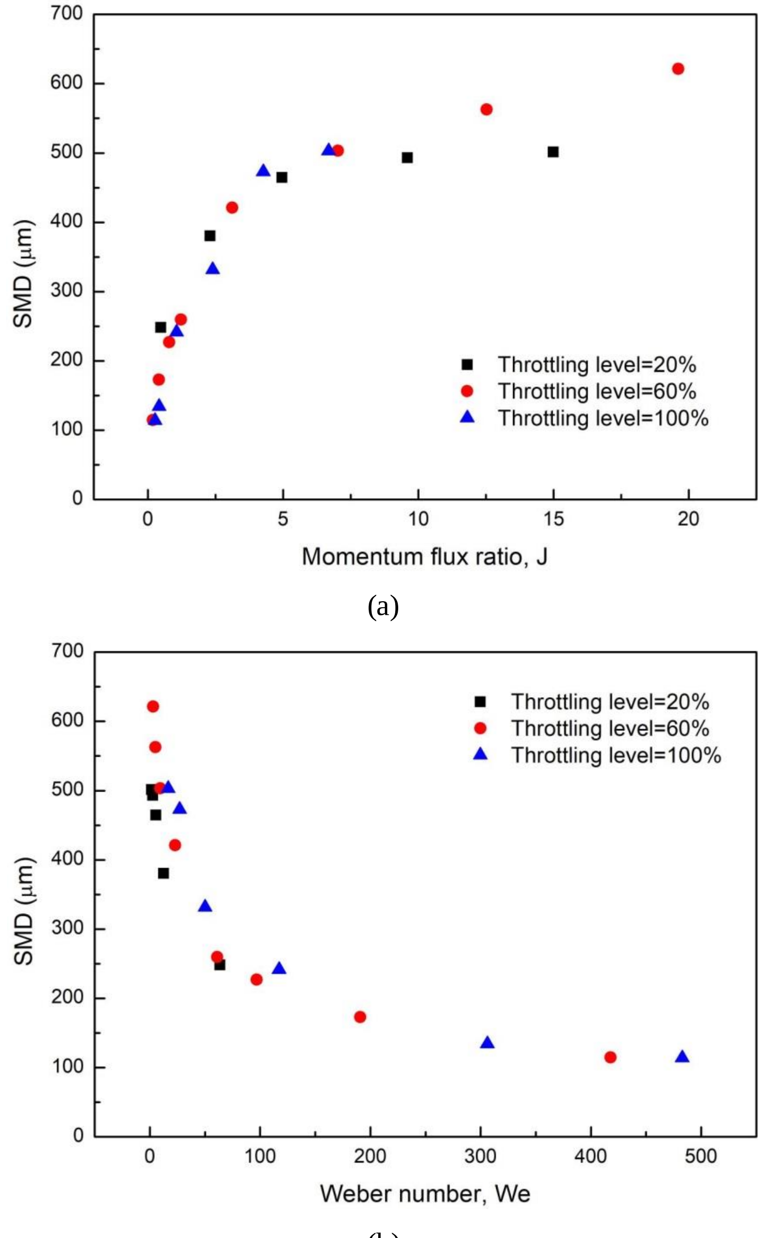

(a)

(b)

Fig. 4.7 Relationship between SMD and (a) momentum flux ratio (J) (b) Weber number (We)

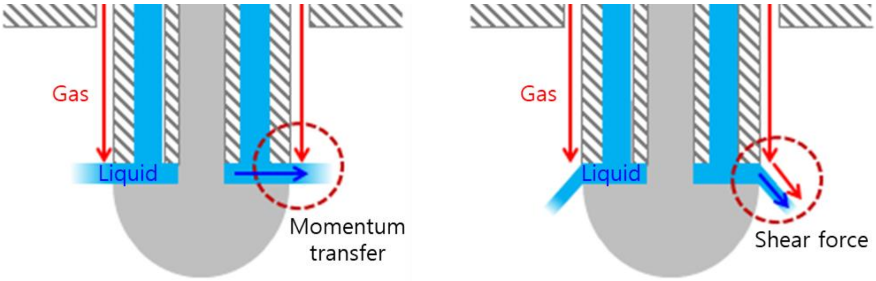

Fig. 4.8 Two breakup mechanisms

At this time, liquid sheet breakup was caused by the transfer of gas momentum. In addition, breakup was sustained by shear force due to the relative velocity between the gas and liquid. Overall, it seemed that complex mechanisms act on breakup.

In Eq. (4.3), when G decreases, the velocity of gas (annular flow) increases, so that the momentum flux of the gas corresponding to the denominator of J becomes relatively strong. Thus, J also decreases as G decreases. In other words, it means that gas momentum transfer, which affects the liquid sheet, generally increased. Therefore, SMD decreased proportionally as J decreased.

For We, when G decreases at each throttling level, the velocity of gas increases; thus, the force corresponding to the numerator of We becomes relatively strong from Eq. (4.4). Namely, it indicates that relative velocity and the deforming force due to the shear force was intensified. Therefore, We and SMD were inversely proportional to each other.

Thus, J and We had opposite proportional relationship to SMD, so SMD can be expressed by the ratio of the these dimensionless numbers. Fig. 4.9 shows the result, where Eq. (4.8) is the final correlation with R^2 = 0.94. In Fig. 4.9, pintle number (P) on the *x*-axis is represented by $J^{-1}We^{1}$ in Eq. (4.8). In the physical sense, P can be expressed as the ratio of the deforming force of the gas that affects the breakup of the droplet and the opposite resistance force of the liquid. As P increased in Fig. 4.9, the deforming force relatively increased and SMD tended to decrease. The correlation will be used to estimate the optimal G to obtain the desired SMD.

$$SMD = -49.48\,ln(P) + 485.99 \tag{4.8}$$

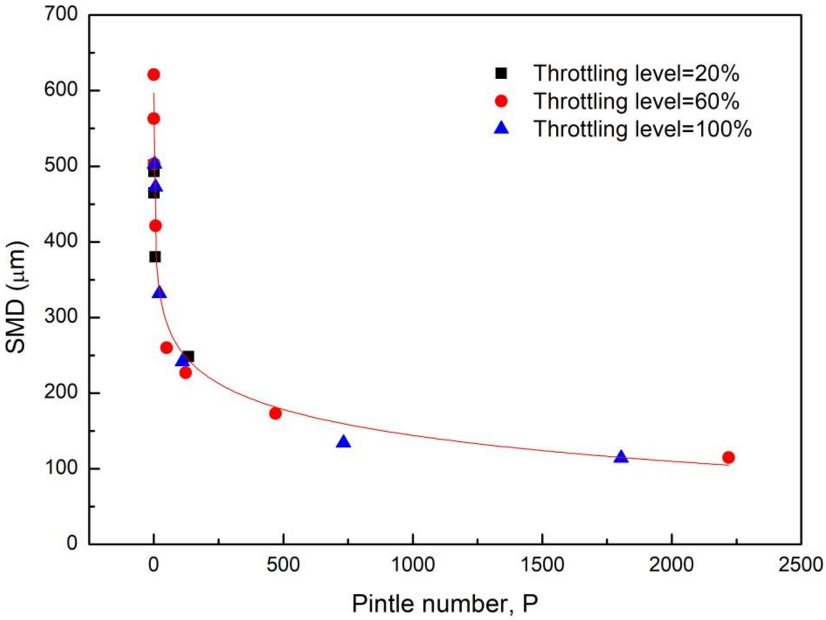

Fig. 4.9 Relationship between SMD and pintle number, $P = J^{-1}\,We^{1}$

4.3.3 Spray Uniformity

Fig. 4.10 shows the radial spray pattern using the optical patternator at the throttling level was 20% and the gap distance was 0.986 mm. The actual spray was injected in a donut form, but in the case of general laser sheet imaging without 2p-SLIPI, signals were detected at the spray center (Fig. 4.10 (a)). On the other hand, when the SLIPI was applied, only the single Mie-scattering signals within the laser sheet were extracted. Fig. 4.10 (c) shows the intensity distribution at the red dot lines in Fig. 4.10 (a) and (b). This showed that conventional light imaging contained many errors such as the multiple scattering even in dense spray.

Using the error correction methods discussed in Section 3.3, spray uniformity was analyzed. To determine uniformity degree, a Patternation Index (PI) and Spray Uniformity Index (SUI) were defined by Eq. (4.9) and Eq. (4.10), respectively.

$$PI(\%) = \sum_{s=1}^{n} \left| \frac{1}{n} - \frac{G_s}{\sum_{s=1}^{n} G_s} \right| \times 100 \tag{4.9}$$

where n and G_s are the number of sectors and intensity of the image per sector, respectively, and

$$SUI = \left[\frac{1}{n} \sum_{s=1}^{n} (y_s - \bar{y})^2 \right]^{1/2} \tag{4.10}$$

where $y_s \equiv \frac{G_s}{\sum_{s=1}^{n} G_s / n}$ and $\bar{y} \equiv \frac{\sum_{s=1}^{n} y_s}{n}$.

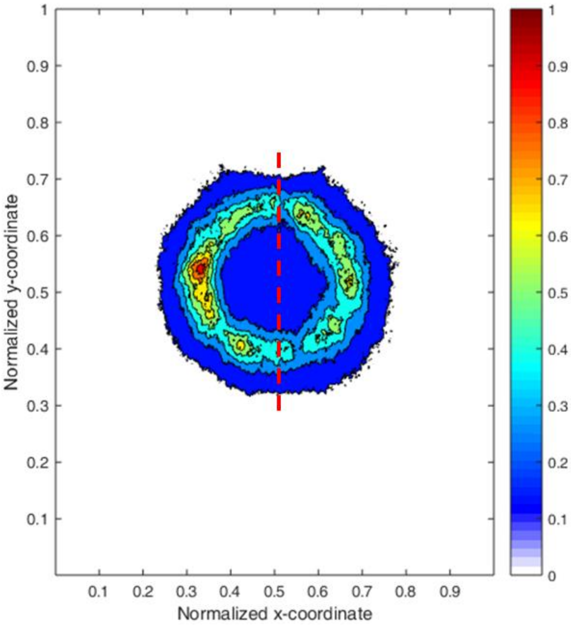
Normalized y-coordinate
Normalized x-coordinate
0.1
0.2
0.3
0.4
0.5
0.6
0.7
0.8
0.9
1
0

(a)

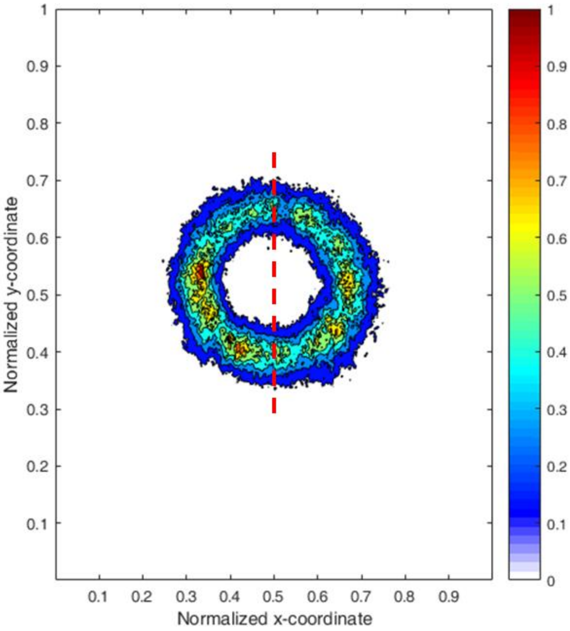
Normalized y-coordinate
Normalized x-coordinate
0.1
0.2
0.3
0.4
0.5
0.6
0.7
0.8
0.9
1
0

(b)

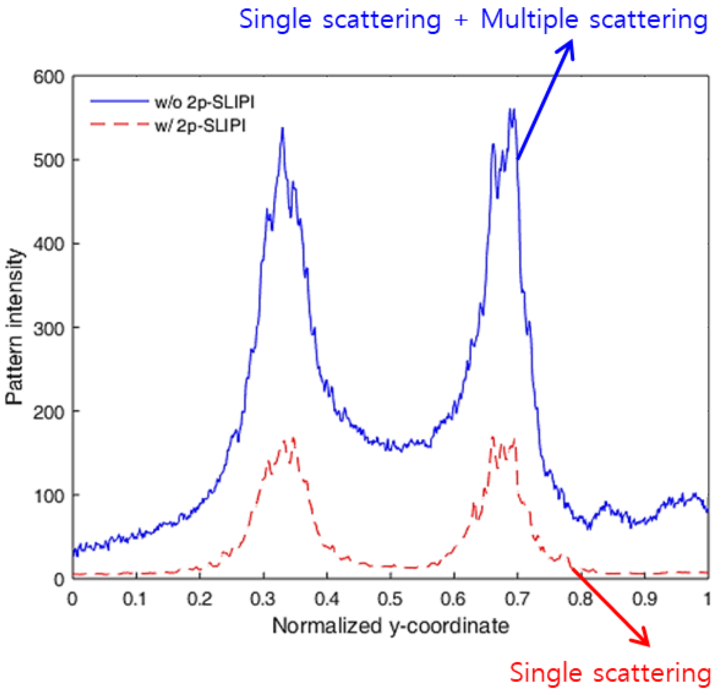

(c)

Fig. 4.10 Results of (a) normalized spray pattern w/o 2p-SLIPI (b) normalized spray pattern w/ 2p-SLIPI, and (c) intensities for red dot lines

PI and SUI represented spray symmetry, circumferential uniformity and standard deviation of the spray distribution [35, 39, 40]. Results of the spray uniformity analysis are shown in Table 4.2. PI, by definition, has a value from zero to 200, and spray uniformity is higher with lower PI. Standard deviations (σ) of PI and SUI with varying G were low at each throttling level. In addition, average standard deviations (σ) of PI and SUI for overall throttling level were 3.62% and 0.04

respectively. From the perspective of SUI, σ appeared to be very small and this meant that the spray uniformity was almost constant irrespective of G and the throttling level. When the spray uniformity associated with PI was expressed as a percentage, and assuming that 100% was the ideal uniform distribution, the average of the spray uniformity from the PI data for the entire throttling levels was about 90%. As an extension of this, average σ of PI data was 1.81%. In this study, when the spray uniformity was more than 90%, based on the average value of PI, and the standard deviation was within 5%, the quality of the injector was considered suitable for experiments.

Table 4.2 Results of uniformity indices at each throttling level

Throttling Level (%)	Avg. PI (σ)	Avg. SUI (σ)
20	19.53 (0.66)	0.3 (0.01)
60	18.43 (2.96)	0.24 (0.05)
100	22.36 (3.97)	0.28 (0.04)

4.3.4 Relationship between Spray Angle and SMD

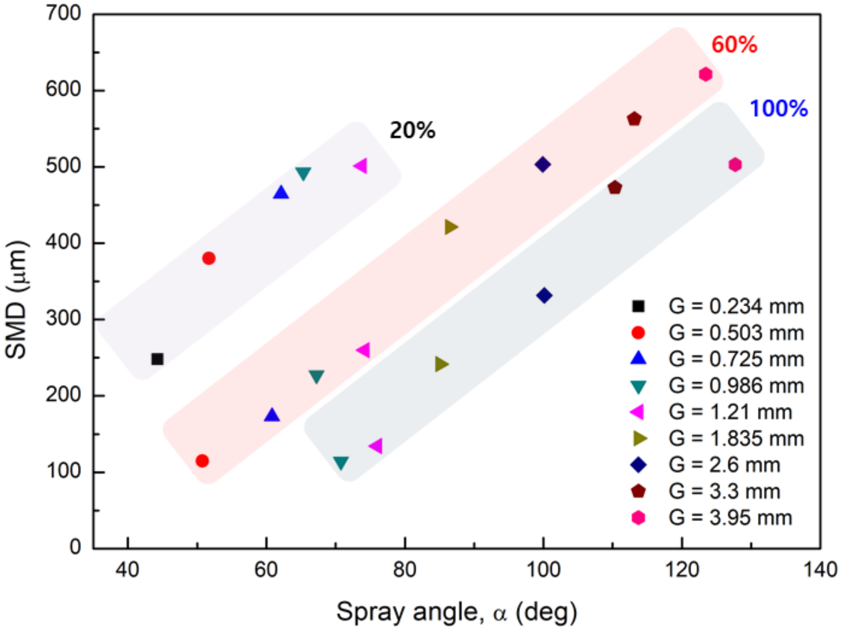

Fig. 4.11 Relationship between SMD and spray angle

Fig. 4.11 shows the relationship between SMD and spray angle for G at each throttling level. SMD and spray angle had a linear relationship at each throttling level. When G was fixed, spray angle was almost constant in the whole thrust range. This is because, as described in Section 4.2.1, the spray angle changed according to G irrespective of the throttling level. In addition, since G and the spray angle were proportional, the spray angle tended to increase when G increased. On the other hand, SMD was different at each throttling level when G was fixed. For example, when G was fixed at 0.986 mm, SMD at the 100, 60, and 20% throttling levels were 114.17, 227.12, and 493.20 μm, respectively. This is because SMD was related not only to G but also to several factors associated with the throttling level as shown in Eq. (4.8). When the throttling level was lowered under the fixed condition of G, SMD increased with J increased and We decreased. This means that with G fixed, the atomization performance deteriorates as the throttling level decreases. Therefore, from the perspective of atomization efficiency, appropriate control range of G was estimated to maintain constant SMD at all thrust levels in Section 4.2.5.

4.3.5 Variations in Gap Distance and Spray Angle with SMD

The control range of G with constant SMD was obtained from an empirical equation (Section 4.2.2). In addition, spray angle variation at the same time was estimated by Eq. (4.7). To analyze the resulting variations, three cases (SMD = 100, 150, and 200 μm) were selected as examples based on ranges typically used in a liquid rocket engine [41].

Fig. 4.12 (a) shows the control range of G required to maintain the corresponding SMD. When SMD was constant, the throttling level and G were linearly related. This indicated that the gas orifice area could be linearly controlled based on throttling level. For liquid, mass flow rate and H also had a linear relationship that controlled outlet area. Therefore, the orifice sizes of liquid and gas could be adjusted linearly for thrust control, respectively.

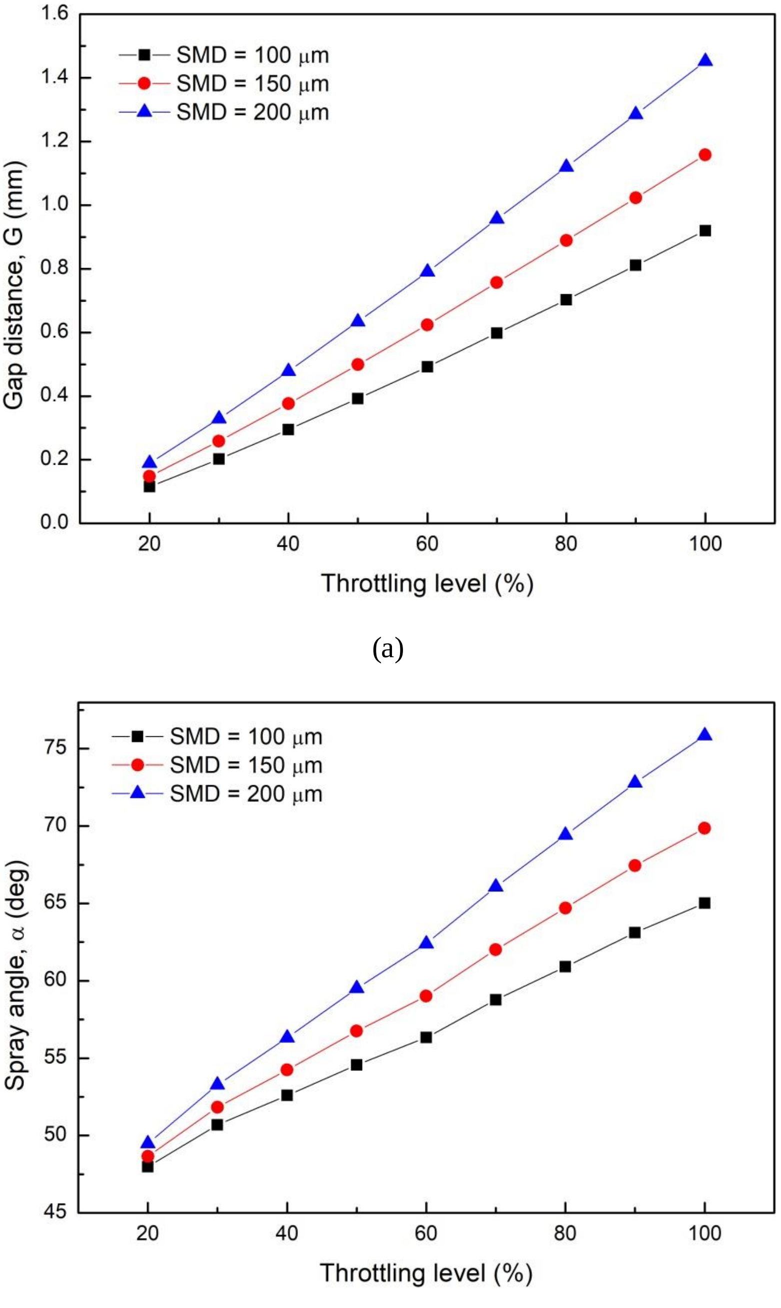

(a)

(b)

Fig. 4.12 Variation ranges of (a) gap distance and (b) spray angle at constant SMD

In addition, as the target SMD became smaller, the overall control range scale decreased. This is because G must be further reduced in order to produce smaller droplets because the gas momentum flux and deforming force must be stronger through increasing the gas velocity.

Fig. 4.12 (b) shows the variation range of the spray angle when G in the corresponding SMD was controlled (Fig. 4.12 (a)). Spray angle also changed linearly with throttling level, and when the target SMD decreased, the change range decreased. This is associated with the results in Fig. 4.12 (a), because the gas momentum was enhanced when G became smaller as SMD decreased.

The results can help predict the G control range to maintain SMD and spray angle variation. Furthermore, these data will be used to develop a control system for the radial and the annular flows.

The original source is from references [42, 43].

CHAPTER 5
SPRAY CHARATERISCIS WITH SKIP DISTANCE

5.1 Background and Objectives

The geometry of the pintle injector is defined using several factors, each of which can influence the spray or combustion characteristics. A critical geometric parameter is the skip distance, which is defined as the ratio of the skip length (L_s) to the pintle diameter (D_p) as shown in Fig. 2.1. If the skip distance (L_s/D_p) is small, the collision of the propellant occurs close to the combustion chamber head; conversely, if the skip distance is large, the annular flow decelerates owing to the friction on the pintle surface [28, 33]. There are several research groups [22, 32, 44-48], with a skip distance of 1 based on reference values. In addition, values of 0.9, 0.75, and 0.375 have been used at Purdue University [13], Tokyo University [18], and Korea Aerospace University [25, 49-51]. Therefore, there appears to be no definitive standard regarding the selection of the skip distance.

Several researchers have attempted to examine the effects of the skip distance. Austin et al. [12] analyzed the combustion performance by changing the geometry for a 667 N class pintle injector engine using nontoxic hypergolic bipropellants. In particular, the skip distance was changed by varying the pintle length from 11.73 mm to 32.05 mm under a constant pintle diameter. It was noted that a smaller pintle length corresponded to a higher performance, likely owing to the increased residence time of the propellant in the combustion chamber. Vasques et al. [15] performed a combustion test while reducing the skip distance from 1 to 0.5 to prevent the heat load on the pintle tip. However, simply reducing the skip distance could not prevent the pintle tip from overheating. Nevertheless, under a skip distance of 1, a deflector mounted on the tip of the pintle exhibited improved cooling. Fang et al. [19] conducted a cold test using water and air as simulants of *LOX* and *GCH4*, respectively. In this test, the pintle diameter was fixed as 30 mm, and the skip distance was changed to 0.25, 0.5 and 1 by varying the skip length. At the same air-water mass flow ratio, no significant difference was noted in the spray angle when the skip distance was 0.25 and 0.5; however, a wider spray angle was noted when the skip distance was 1, likely because of the decrease in the air velocity. In addition, the numerical analysis of the actual propellant indicated that the combustion efficiency increased up to the point at which the skip distance was near 1 and then decreased. Chang et al. [52] numerically characterized the temperature and combustion efficiency against the skip distance for a 500 N class *GOX* /*GCH4* engine model with a two-row hole type pintle injector. The pintle diameter was fixed at 11 mm, and the skip distance was changed between 0.64 and 1.5 by changing the skip length between 7 and 16.5 mm. As the skip distance increased, the pintle surface temperature reduced by more than 20%, and the temperature near the pintle tip and in the head recirculation zone also decreased. Moreover, the combustion efficiency exhibited a deviation of less than 0.2% and was thus barely affected by the skip distance. Huang et al. [53] investigated the effect of the skip length on a continuous rotating detonation wave in a hollow chamber equipped with a pintle injector with gaseous H_2/air as a propellant. The skip length was adjusted from 0–20 mm at 5 mm intervals, and the pintle diameter was fixed at 90 mm. It was noted that the generation of the continuous rotating detonation wave was suppressed as the skip length increased, likely because of the increase in the head recirculation zone. Similar trends were observed when ethylene/air was used under the same chamber and skip length conditions as those used in [53]. However, in the section in which the skip length increased from 10 mm to 15 mm, the operation range of the continuous rotating detonation wave was extended, and the main propagation mode was deformed [54].

These studies indicate that the skip distance is a key geometric factor that influences the spray and combustion field formation, thereby affecting the engine performance. However, previous studies did not provide sufficient details regarding the selection of a specific skip distance. In addition, only a few studies have been focused on the skip distance, and thus, a database to establish the correlations of the key parameters of pintle injectors is lacking. In particular, the correlation between the skip distance and the spray characteristics remains unclear. Because the atomization efficiency of a pintle injector is related to the combustion characteristics and affects combustion performance [26], it is essential to analyze the spray characteristics.

Therefore, cold flow tests were conducted, focusing on the skip distance, to establish the correlation of this parameter with the spray characteristics. The spray angle and SMD were experimentally observed with changes in the skip distance. In addition, the velocity distribution trend of the annular flow near the pintle surface was numerically analyzed.

5.2 Experimental Conditions

Table 5.1 Experimental conditions for skip distance

Liquid Mass Flow Rate (g/s)	16.68–83.53
Gas Mass Flow Rate (g/s)	1.99–9.95
Outlet Height (mm)	0.1–0.6
Gap distance (mm)	0.858
Pintle diameter (mm)	11
Liquid Pressure Drop (MPa)	0.02–0.22
Gas Pressure Drop (MPa)	0.01–0.12
Skip length (mm)	2.75, 4.5, 10, 15.5, 21
Skip distance	0.25, 0.41, 0.91, 1.41, 1.91

Table 5.1 lists the main parameters of the pintle injector shown in Fig. 2.1. The objective was to control the thrust in a range of 20–100% in intervals of 20%. H was adjusted from 0.1 to 0.6 mm and G was fixed to eliminate its influence on the spray characteristics. This G was chosen for the interpolation of SMD's data points obtained in Chapter 4 as SMD was about 200 μm in throttling level of 60%. The skip distance was changed by adjusting L_s while maintaining the pintle diameter at a constant value. L_s was adjusted by moving the pintle post part shown in Fig. 5.1 up and down along the central axis of the pintle injector. Accordingly, the skip distance was adjusted from 0.25 to 1.91, and the corresponding spray characteristics were examined at each throttling level.

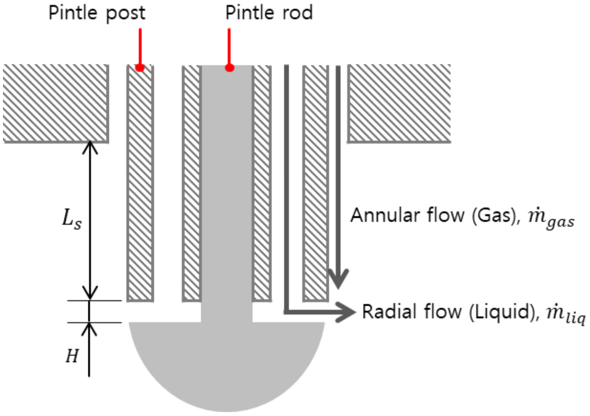

Fig. 5.1 Cross-sectional view of pintle injector

5.3 Numerical Conditions and Setups

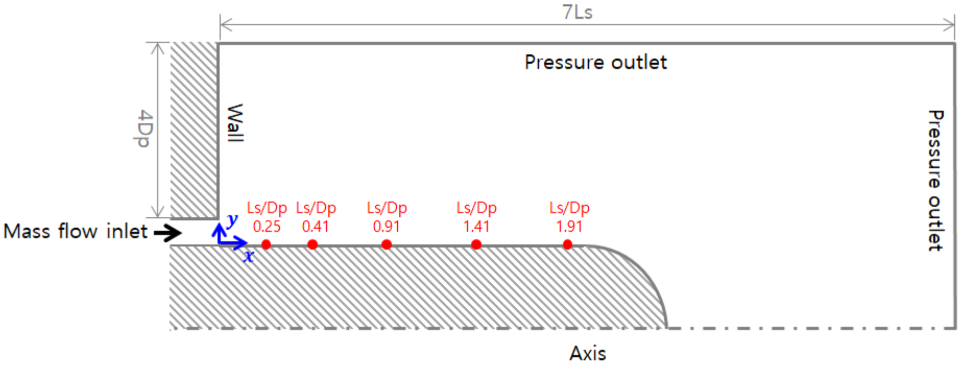

Fig. 5.2 Computational domain

The spray characteristics such as the spray angle and *SMD* changed with the change in the gas velocity with the skip distance. Therefore, to analyze the relationship between the gas velocity field and the spray characteristics, the gas velocity field near the pintle surface was numerically analyzed. The numerical analysis was performed using the STAR-CCM+ software developed by SIEMENS. Three throttling levels of 20%, 60% and 100% under the steady state condition were considered. Fig. 5.2 shows the 2D axisymmetric computational domain and boundary conditions. The air mass flow rate corresponding to each throttling level was used for the input condition, and the pressure outlet corresponded to the atmospheric condition. For the mesh, a trimmed cell mesher was used, and through convergence tests, a total of 67,805 cells with a refinement level of 5 applied near the pintle surface were generated. The segregated flow model was used to solve the uncoupled flow equations for velocity and pressure. The realizable k-epsilon model with a high y+ wall treatment was used.

5.4 Results and Discussion

5.4.1 Spray Angle

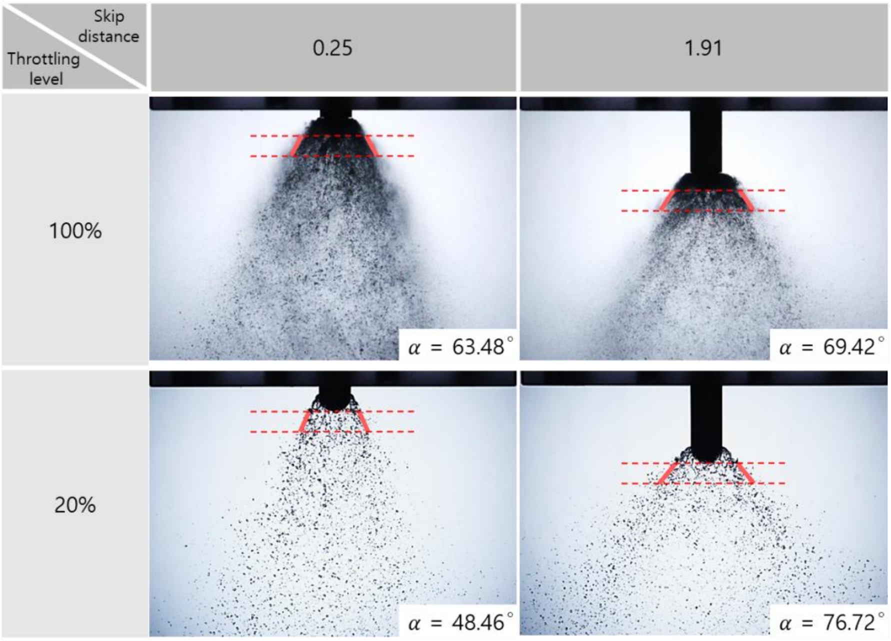

Fig. 5.3 Spray angle under different skip distances and throttling levels

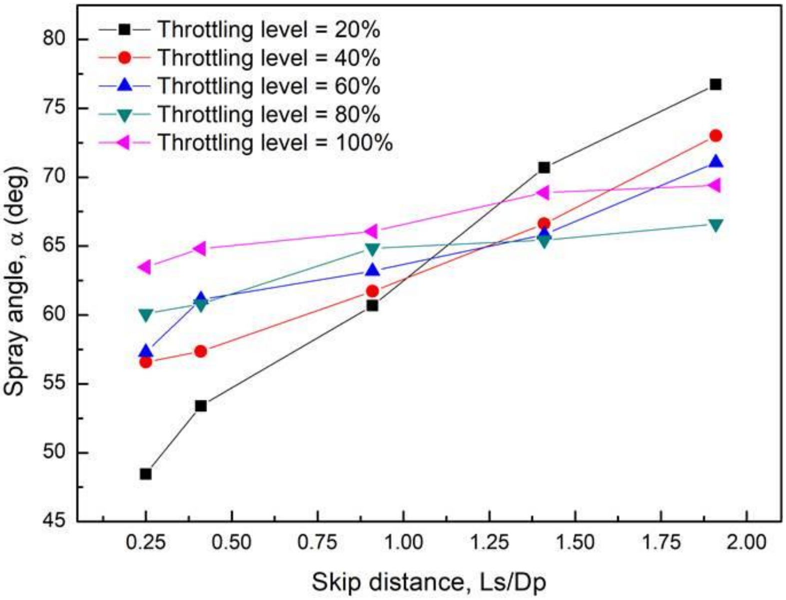

(a)

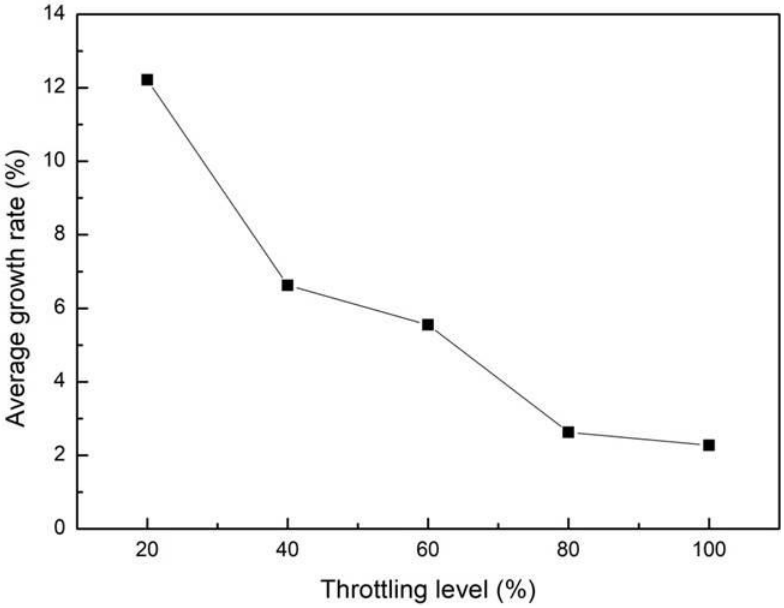

(b)

Fig. 5.4 Results for the (a) spray angle and (b) average growth rate of spray angle

Fig. 5.3 shows the spray patterns obtained using backlight photography. The red line in Fig. 5.3 represents the obtained spray angle and spray angle measurement region on a raw image. As the skip distance increased from 0.25 to 1.91, the spray angle at each throttling level gradually increased. This finding indicates that even if the outlet orifice area of the radial and annular flows was fixed, the spray characteristics changed with the change in the skip distance.

The variations in the spray angle for all the experimental conditions are shown in Fig. 5.4 (a). For all the throttling levels, the spray angle increased in proportion to the skip distance. This phenomenon likely occurred because as the skip distance increases, the skip length, which is the distance of movement of the gas, increases before the gas collides with the liquid. Consequently, because the momentum loss rate of the gas gradually increases owing to the friction of the pintle post surface, the spray angle becomes relatively large.

When considering the relation between the skip distance and the spray angle, the average growth rate according to the throttling level was also examined, as shown in Fig. 5.4 (b). The average growth rate was obtained by calculating the growth rate between the experimental data points for five skip distances at each throttling level. In other words, growth rate_1 was obtained for the interval corresponding to skip distances of 0.25 and 0.41, and growth rate_2 pertained to the interval between the skip distances of 0.41 and 0.91; The average growth rate was obtained by averaging four growth rates. It was noted that as the throttling level decreased, the average growth rate of the spray angle was relatively high. In particular, when the throttling level was 20%, the average growth rate was extremely high (12.21%), approximately 5.38 times compared to that at the throttling level of 100%. As shown in Fig. 5.3, the maximum difference in the spray angle corresponding to the skip distances of 0.25 and 1.91 was 28.26° and 5.94° for throttling levels of 20% and 100%, respectively. Thus, it was concluded that the effect of the skip distance on the spray angle was more pronounced under a low throttling level, as discussed in section 5.3.3.

5.4.2 Droplet Size (SMD)

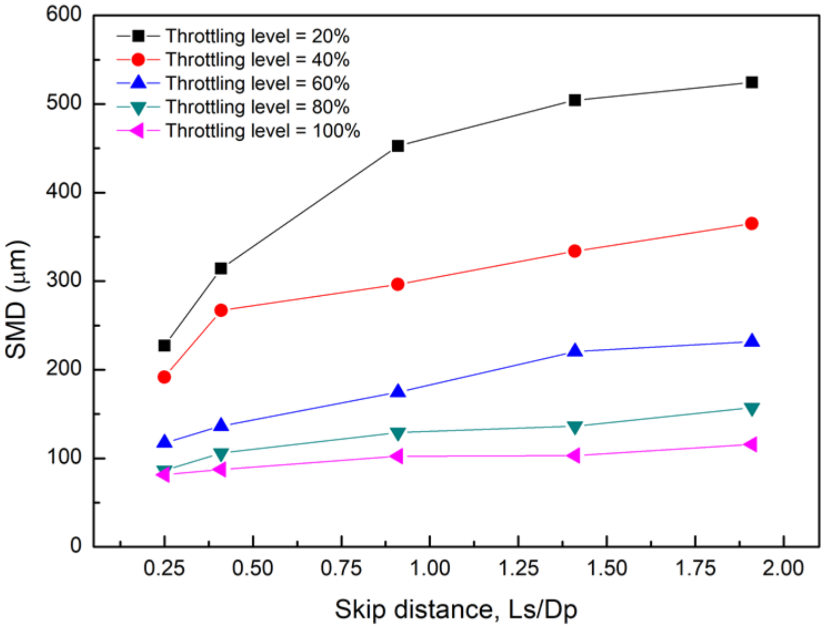

Fig. 5.5 SMD with skip distance

Fig. 5.5 shows the variations in the SMD according to the skip distance. Similar to the spray angle, SMD tended to decrease when the skip distance decreased, likely because of the increase in the aerodynamic force affecting the breakup. In contrast, an increase in the skip distance likely caused the atomization efficiency to decrease owing to the larger SMD. This trend can be more clearly observed in Fig. 5.6.

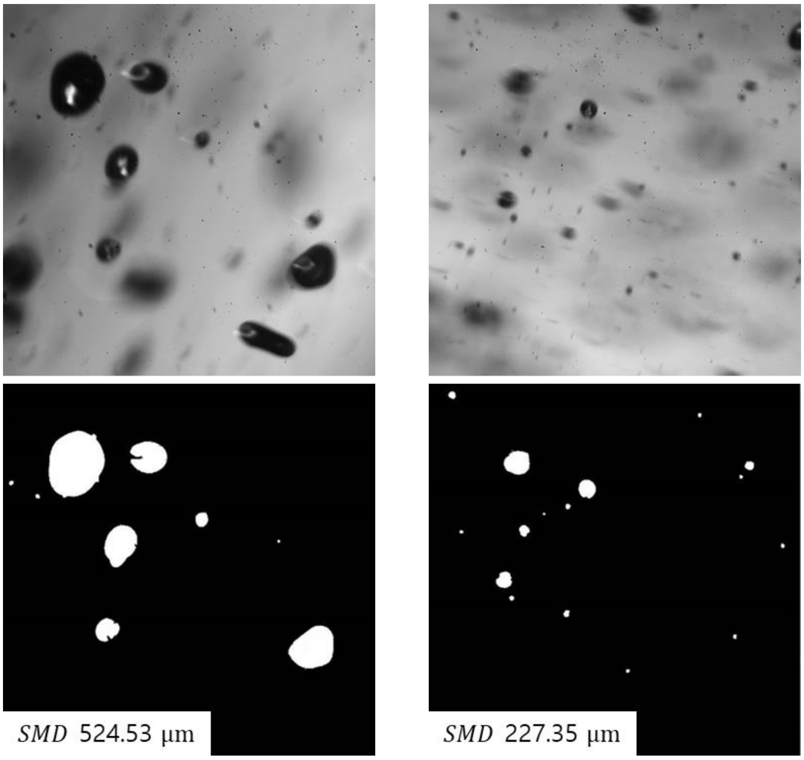

(a) (b)

Fig. 5.6 Grayscale and binary images of droplets at throttling level of 20% with skip distance of (a) 1.91 and (b) 0.25

Moreover, SMD was more sensitive to the skip distance at a lower throttling level. In particular, the variation of SMD was the largest at a throttling level of 20%. At throttling levels of 100% and 20%, the differences between the skip distances of 0.25 and 1.91 were 34.24 μm and 297.19 μm, respectively. The average growth rate for the SMD was 9.34% and 24.42% at throttling levels of 100% and 20%, respectively. These findings indicate that a lower throttling level corresponded to a larger change in the aerodynamic force owing to the skip distance. In other words, when the gas velocity at the outlet of the orifice was smaller, owing to the low throttling level under the same geometry conditions, the change rate of the velocity was larger during movement along the skip length.

5.4.3 Distribution of Gas Velocity

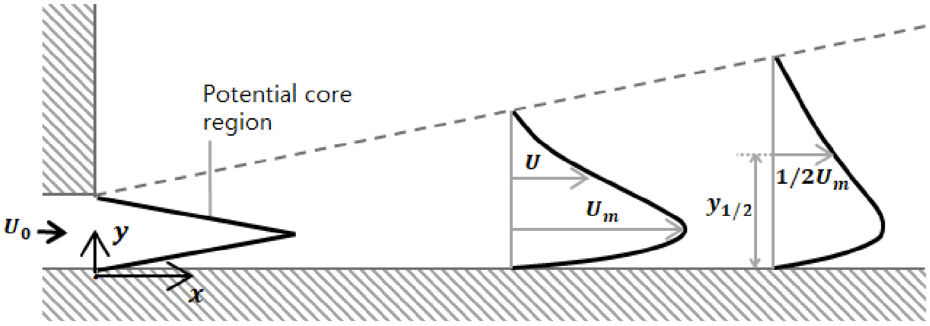

Fig. 5.7 Schematic of turbulent wall jet flow [55]

In the pintle injector, gas is injected through a specific G and flows in open air along the pintle surface. Thus, the flow region near the pintle surface is similar to that of a wall jet flow. The velocity profile in x-axis of a turbulent wall jet flow is as shown in Fig. 5.7. A potential core region exists in which the orifice exit velocity remains constant without being affected by the surrounding environment. Then, as the gas progresses further along the axial direction (x-axis), the velocity distribution widens and decreases, owing to friction at the pintle surface and mixing with ambient air. Finally, the profile becomes geometrically similar in the developed region, where the axial velocity (U) initially increases from the wall (zero) to a maximum value (U_m) at a certain vertical distance (y). Subsequently, the axial velocity tends to decrease [55, 56].

Fig. 5.8 shows the numerical results of the gas velocity field under different throttling levels. It was found that the potential core region existed from the origin. The gas velocity distribution at each skip distance is shown in Fig. 5.9. The initial velocity at x = 0 was maintained in the regions in which the skip distance was relatively small. To analyze this potential core region for each throttling level, the end of the region was considered as the axial (x-axis) point at which the initial velocity decreased by 95% [57]. Fig. 5.10 shows U profile at the line where x is 0 to 21 mm with y is $G/2$ for throttling level of 20% and 100%. It can be seen that when the throttling level was 100% compared to 20%, the velocity in the inlet was maintained relatively longer. After specific potential core length, the velocity gradually decreased.

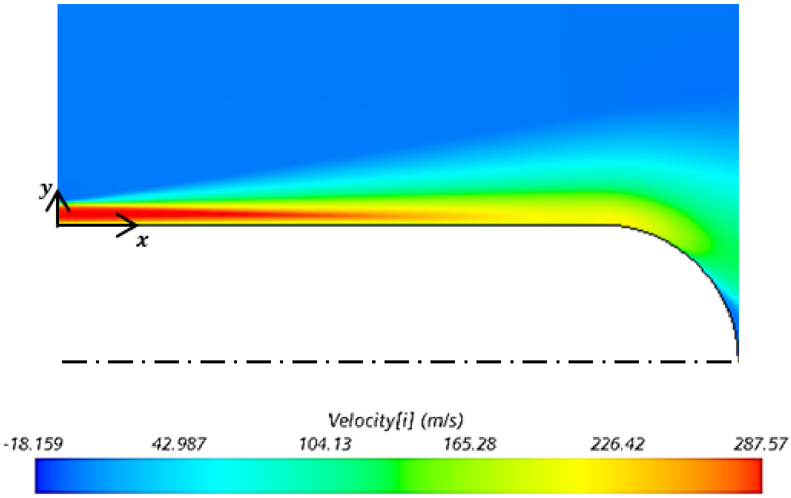

(a)

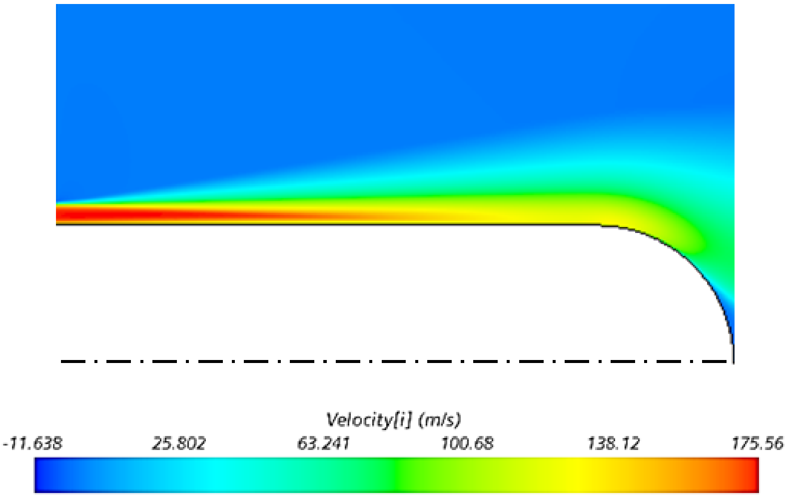

(b)

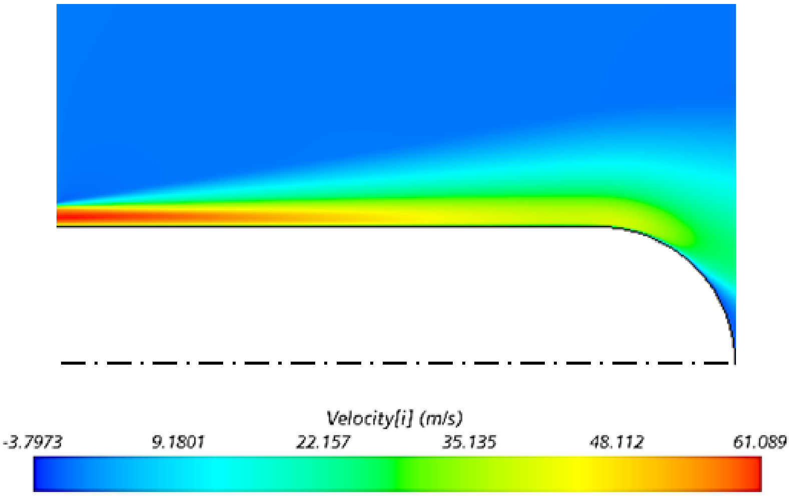

(c)

Fig. 5.8 Velocity (x-axis) field with throttling level of (a) 100%, (b) 60%, and (c) 20%

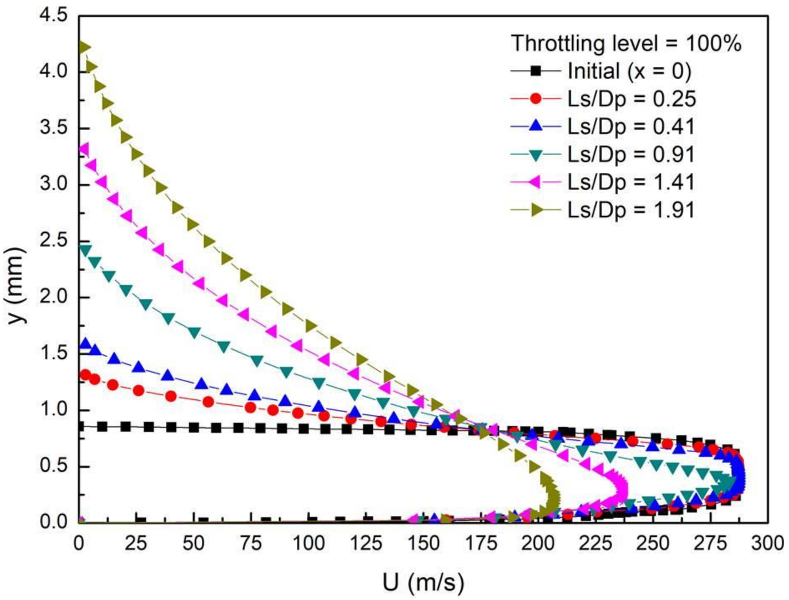

(a)

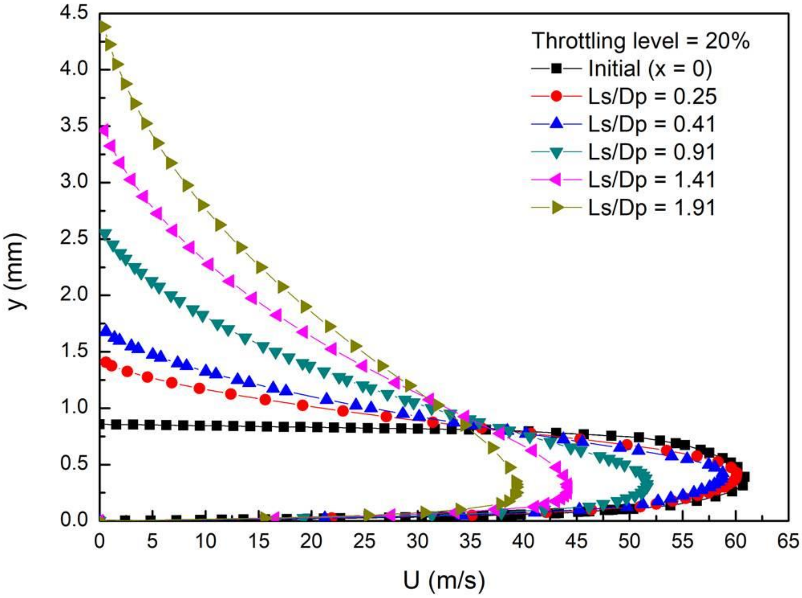

(b)

Fig. 5.9 Velocity profile in *x*-axis with throttling level of (a) 100% and (b) 20%

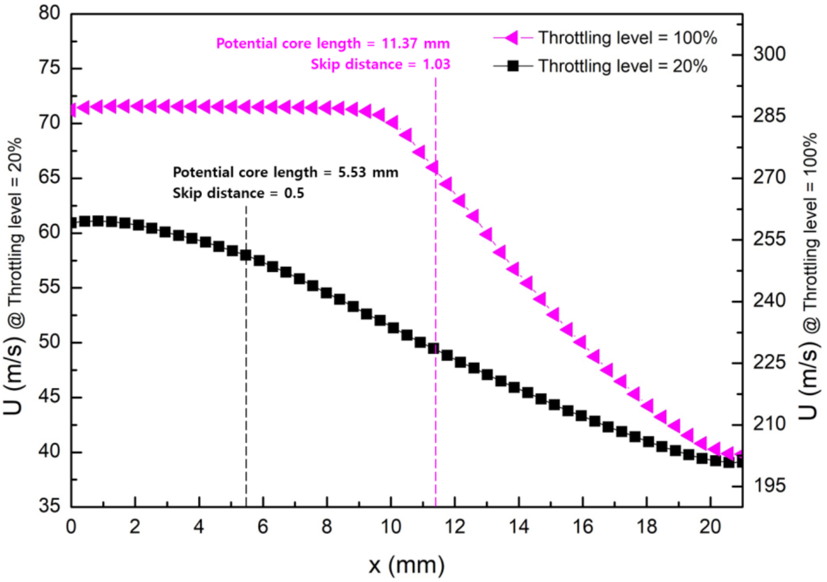

Fig. 5.10 Velocity profile in *x*-axis at $y = G/2$

Table 5.2 shows the potential core length for the throttling level of 20%, 60%, and 100% and the corresponding skip distance.

Table 5.2 Potential core length

Throttling Level (%)	**100**	**60**	**20**
Potential Core Length (mm)	11.37	10.5	5.53
Skip distance, L_s/D_p	1.03	0.95	0.5

As the throttling level decreased, the potential core length and corresponding skip distance decreased. This trend was clearly seen in Fig. 5.8. Therefore, if the initial gas velocity decreased, i.e., under a low throttling level, the gas was considerably influenced by the surrounding conditions as the gas moved downstream. However, as the gas initial velocity increased, the initial condition was more dominant than the surrounding conditions. In particular, the change in the potential core end point was large at a throttling level of 20%. Therefore, the velocity distribution decayed more rapidly after the potential core. This gas velocity distribution trend indicates that the aforementioned changes in the spray angle and SMD were the greatest at the throttling level of 20%.

After the potential core region in Fig. 5.9, the gas distribution became similar to the velocity profile in the developed region shown in Fig. 5.7. For this region, Fig. 5.11

shows the similarity when U and y are considered in the dimensionless form by U_m and $y_{1/2}$, respectively, where U is half of U_m in each case. The figure also shows the velocity profile based on Eq. (5.1) proposed by Verhoff [58] for turbulent wall jet flow. They results indicated good agreement, and it was noted that U/U_m first increased to a value of one and later decreased.

$$U/U_m = 1.48\left(y/y_{1/2}\right)^{1/7}\left[1 - erf\left\{\, 0.68\left(y/y_{1/2}\right)\right\}\right] \qquad (5.1)$$

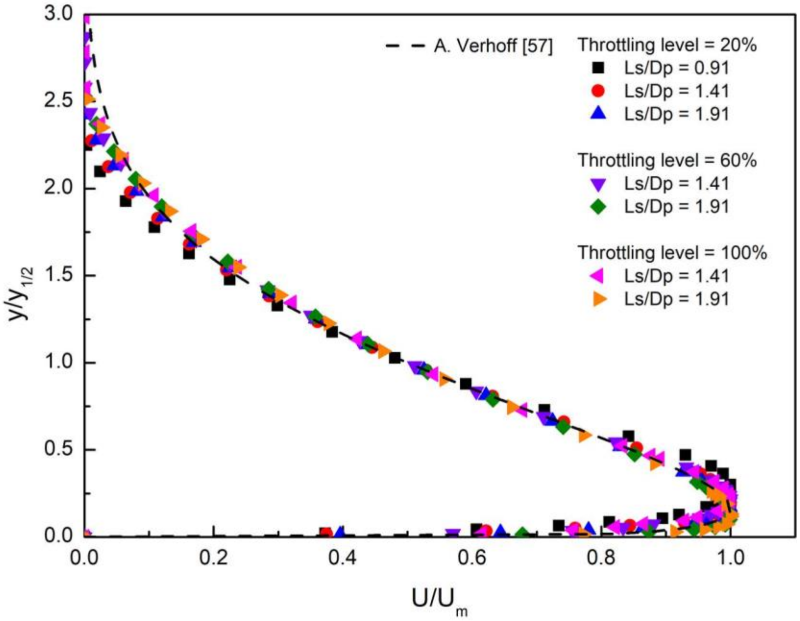

Fig. 5.11 Similarity of velocity in the *x*-axis

The variations in the spray characteristics are fundamentally related to the changes in the gas velocity with changes in the skip distance and throttling level. Therefore, the variations in the gas velocity were examined in terms of the decay rate of U_m (Dr) at each x point (Eq. (5.2)). In particular, the decay rate indicates the amount of decrease in the gas velocity as it flows downstream, with reference to the initial point (x = 0).

$$Dr = \left(U_{m,x=0} - U_m\right)/U_{m,x=0} \tag{5.2}$$

Fig. 5.12 (a) shows the percentage decay rates under different conditions. As the gas moved downstream, i.e., with increase in the skip distance, the decay rate increased. The gas velocity changed with the skip distance owing to the interaction with the pintle surface and surrounding air, as mentioned previously. Moreover, when the throttling level decreased, the variation range of the decay rate with the skip distance was relatively large, likely owing to the shorter potential core. In particular, at a throttling level of 20%, the decay rate was relatively high owing to the fastest transition from the potential core to the developed region.

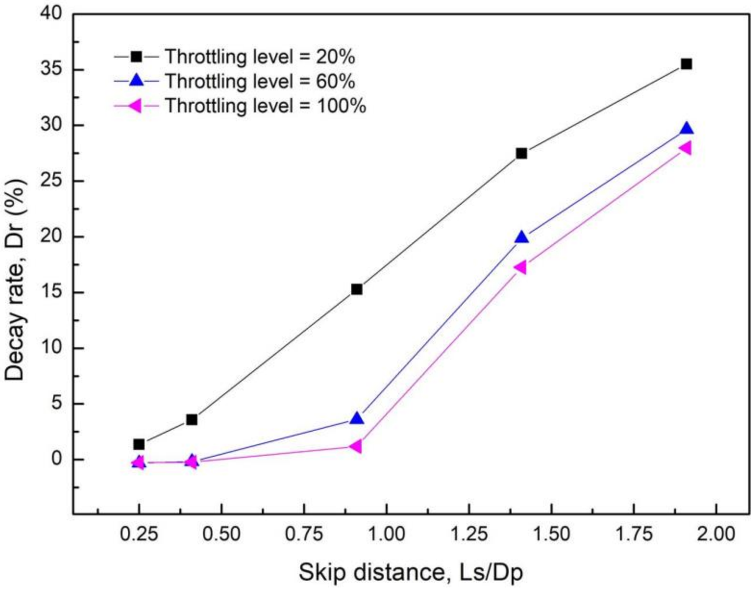

(a)

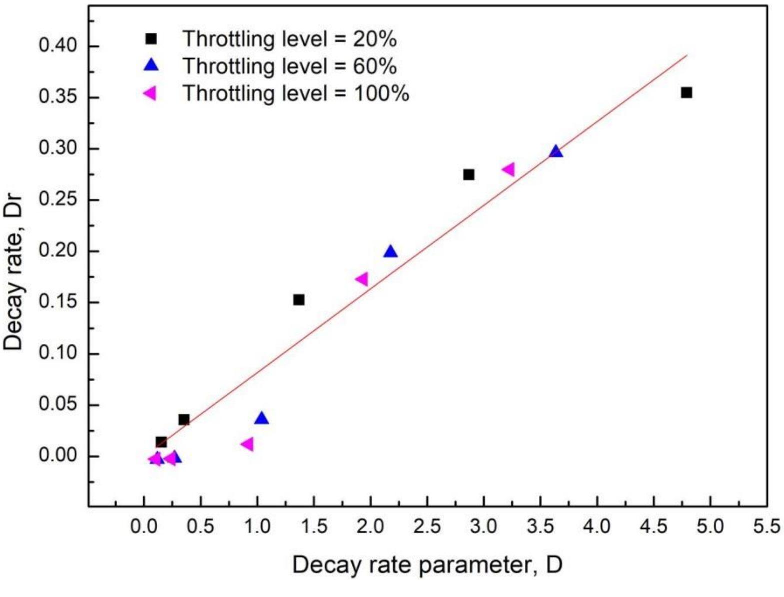

(b)

Fig. 5.12 Decay rate with (a) skip distance (b) decay rate parameter

The decay rate was related not only to the skip distance but also to the throttling level. As described above, the decay rate was proportional to the skip distance and inversely related to the throttling level. Thus, the trend of the decay rate was expressed as a function of the decay rate parameter (D), as shown in Eq. (5.3), which involved L_s/D_p and H/G, terms related to the skip distance and throttling level, respectively.

$$D = (L_s/D_p)^{1.69}(H/G)^{-0.22} \tag{5.3}$$

Finally, the variations of decay rate was expressed as one trend as in Eq. (5.4), with R^2 = 0.95 (Fig. 5.12 (b)).

$$Dr = 0.08D \tag{5.4}$$

5.4.4 Correlations of Spray Characteristics with Decay Rate

In Chapter 4, the skip distance was fixed as 1, and the spray angle had a linear relationship with the kinetic energy ratio (K), which involved the total momentum ratio (TMR) and H/G. When determining TMR, which is closely related to the spray angle of the pintle injector, the value of V in Eq. (4.5) was considered at the exit of each fluid orifice. The relationship between the spray angle and K was expressed as in Eq. (4.7).

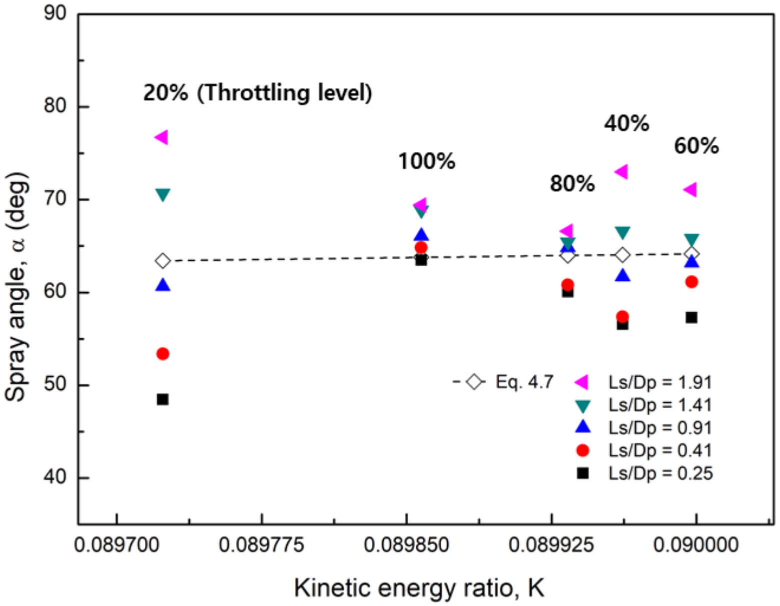

Fig. 5.13 Spray angle with kinetic energy ratio, $K = TMR\ (H/G)$

Because the effect of the skip distance was not considered, TMR remained constant even when the skip distance changed. Also, since $K \propto f(G)$, it can be seen that K was almost constant at all throttling levels under experimental condition where G was fixed. Therefore, the spray angle was almost the same for all throttling ranges from Eq. (4.7). These results can be seen in Fig. 5.13. When the graph was plotted in relation to only K and the spray angle, Eq. (4.7) yielded only one spray angle regardless of the skip distance.

Nevertheless, in this Chapter, the spray angle was determined in terms of the decay rate (Dr), which is related to the skip distance. The corresponding results are shown in

Fig. 5.14, with the correlation derived using Eq. (5.5), with R^2 = 0.94.

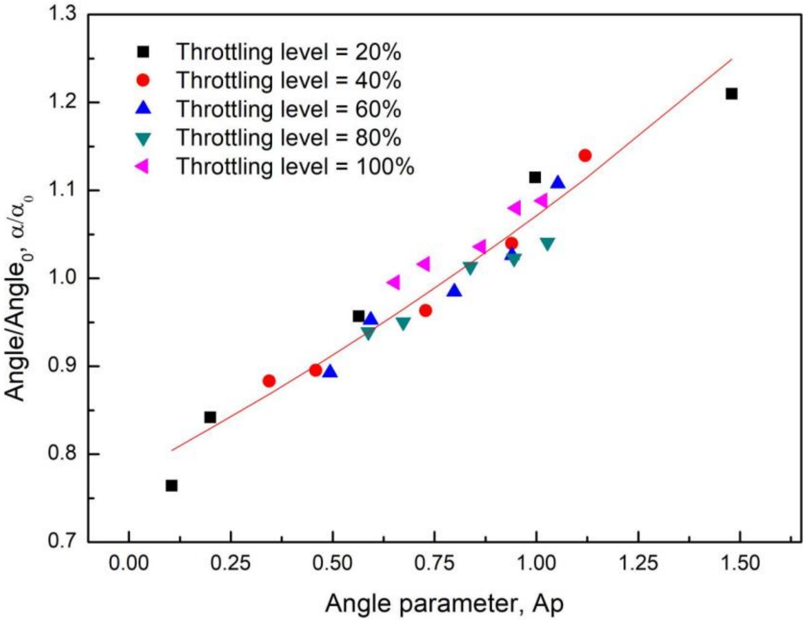

Fig. 5.14 Relationship between $Angle/Angle_0$ and angle parameter, $Ap = (4.25\ Dr)^{TMR}$

From now on, subscript 0 means the value when the skip distance is 1. The spray angle was normalized by α_0 (Eq. (4.7)), and the angle parameter (Ap) was expressed as $(4.25Dr)^{TMR}$. It had the form of power between the gas velocity decrease and momentum ratio. As the gas moves down at each throttling level, TMR associated with the spray angle is fixed. The decay rate increases accordingly and the spray angle becomes wider. So the change rate of the spray angle with Ap increased as shown in Fig. 5.14. This calculation allowed the estimation of the variation in α_0 with the skip distance.

$$\alpha/\alpha_0 = 0.78\, exp(0.32Ap) \tag{5.5}$$

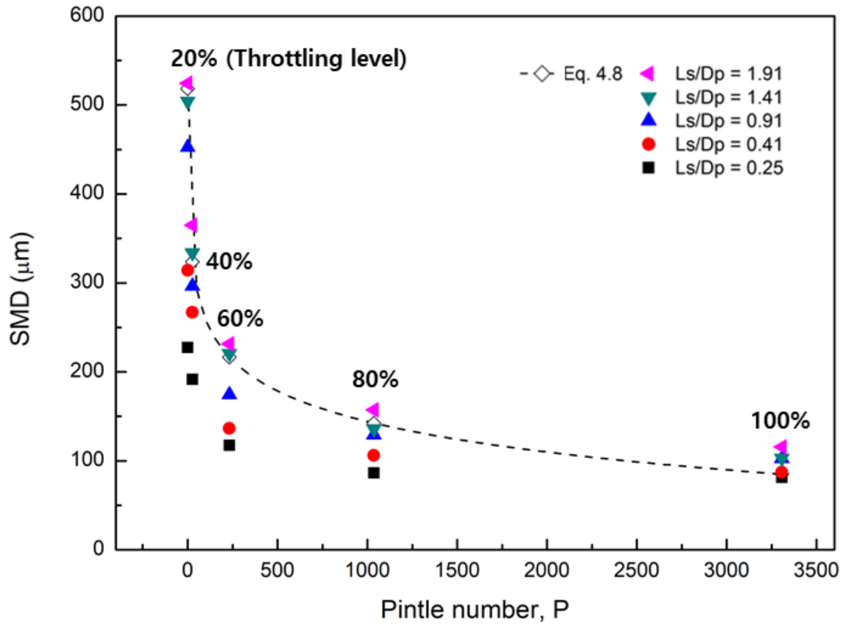

Fig. 5.15 SMD with pintle number, $P = J^{-1}\, We^{1}$

Similar to the spray angle, in Chapter 4, the correlation for SMD was as shown in Eq. (4.8). In this case as well, V was obtained at the outlet of the orifice, and only one value was estimated at each throttling level, as shown in Fig. 5.15.

In this Chapter, the change rate of SMD with the skip distance was considered, and the correlation was as shown in Fig. 5.16. SMD, normalized using SMD_0 (Eq. (4.8)), was related to SMD parameter (Sp) according to Eq. (5.6) with R^2 = 0.81.

Sp was defined as $(0.2\, J^2\, We)^{exp(-3.6\, Dr^{\,0.2})}$. In the case of SMD, when the gas moves along the axial direction at each throttling level, $J^2\, We$ related to breakup is fixed and the decay rate increases as the gas velocity decreases gradually. The decay rate was proportional to SMD, so the trend between Sp and change rate of SMD was like Fig. 5.16.

$$SMD/SMD_0 = 1.29\, Sp^{-0.44} \tag{5.6}$$

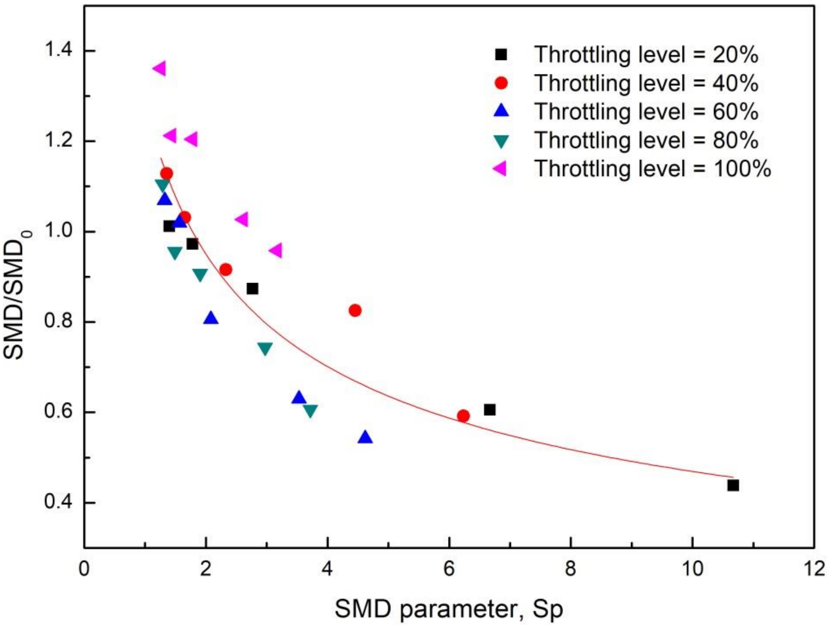

Fig. 5.16 Relationship between SMD/SMD_0 and SMD parameter, $Sp = (0.2\, J^2\, We)^{exp(-3.8\, Dr^{\,0.5})}$

5.4.5 Trends of Average Spray Angle and SMD with Standard Deviation

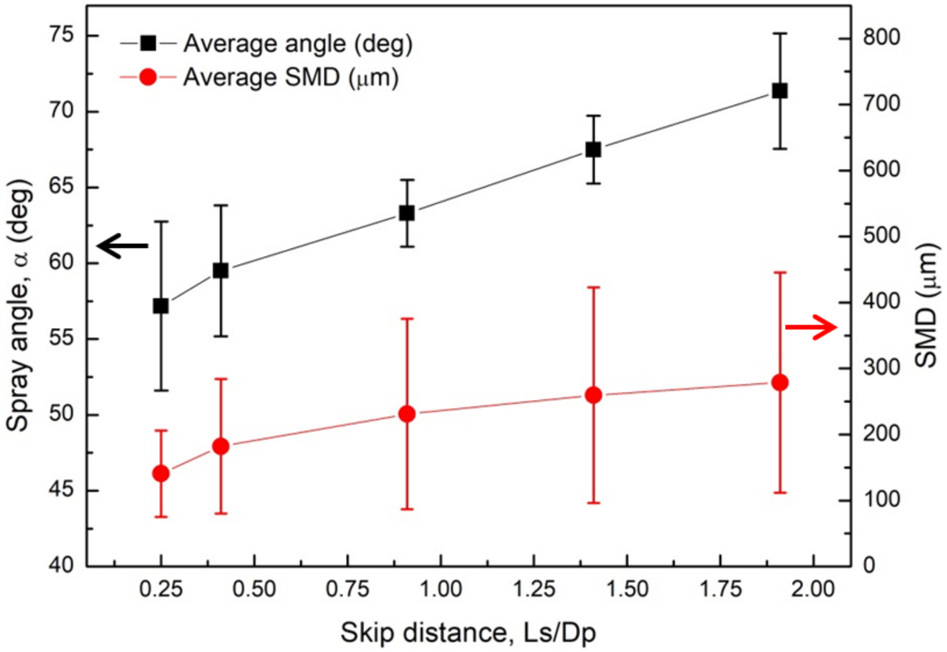

Fig. 5.17 Average spray angle and SMD with standard deviation

Fig. 5.17 shows the average and standard deviation of the spray angle and SMD for throttling levels ranging from 20–100% for each skip distance. Overall, the average values increased with the skip distance. The standard deviation of the spray angle tended to decrease gradually and then increase. The standard deviation of the SMD continued to increase with the skip distance.

To achieve a high spray performance, SMD must be relatively small, and thus, a small skip distance is preferable. In addition, the smaller droplet, the better result can be obtained by reducing the incidence of heat flux peak at the combustion chamber wall [59]. However, an excessively small skip distance may lead to excessive thermal load on the combustion chamber head. In this case, since the spray angle becomes narrow, thermal load may occur in the pintle tip, and the reaction rate may decrease as the central recirculation zone decreases [24].

Therefore, a proper trade-off is required when determining the skip distance. Along with the skip distance, the geometric factors H and $G,$ which are associated with the control of the orifice of the fluids affect the spray characteristics. Nevertheless, if these oincethree geometric factors are independently controlled to obtain the optimum spray performance in each condition, the system complexity increases. Thus, from the design point of view, the method of controlling H and G with a fixed skip distance was considered. The skip distance corresponding to the lowest standard deviation was considered because this value corresponds to the spray characteristics in the entire thrust range being as constant as possible. Because SMD standard deviation tended to continuously increase, as mentioned previously, the proper skip distance was considered in terms of the standard deviation of the spray angle. Therefore, under the experimental conditions, the appropriate skip distance was noted to be approximately 0.91. Considering that the skip distance was typically around 1 in the reference [28], it can be seen that the range was obtained at a similar level.

CHAPTER 6
CONCLUSION

Liquid/gas pintle injector for a 400 N class small thruster was designed and research was conducted to derive optimal design parameters. The developed pintle injector adopted the continuous slit type to achieve a uniform spray pattern. In addition, guide wall was applied to radial flow internal passage to maintain the concentricity of the pintle rod. In the annular flow passage, the distribution plate was mounted inside the manifolds so that it could be evenly distributed.

The primary focus was the control range of the annular flow's orifice area. For this, gap distance related to the annular flow's orifice area was selected as a representative parameter, various down manifolds were fabricated, and spray characteristics were observed by replacing the down manifold at each thrust level. Spray angle was linearly related to the total momentum ratio. As gap distance decreased under a fixed flow rate condition, the annular flow momentum intensified due to the increased annular flow velocity, which in turn decreased the total momentum ratio and narrowed spray angle. Kinetic energy ratio, which had a high correlation with spray angle throughout the thrust range, was defined by introducing the ratio of outlet height associated with the radial flow's outlet area to gap distance in the total momentum ratio, and a correlation equation was subsequently developed. The Sauter mean diameter was related to both momentum flux ratio and Weber number. The empirical correlation for Sauter mean diameter was obtained. From the spray characteristics results, the gap distance control range to maintain a constant Sauter mean diameter over the entire thrust range was calculated based on atomization efficiency. Furthermore, the gap distance was linearly controlled by throttling level.

The second part was an analysis of variation in the spray characteristics with the skip distance. The skip distance is geometric parameter related to the moving distance of the annular flow along the pintle surface. It is important factor influencing the spray characteristics. From the experimental results, the spray angle and SMD tended to increase as the skip distance increased. In particular, the variation in the spray characteristics was large at a throttling level of 20%. To further analyze these trends, the gas velocity distribution was numerically analyzed. It was noted that the velocity profile exhibited a potential core near the orifice, post which, a similarity was observed. Overall, the gas velocity was noted to be more affected by the ambient conditions at lower throttling levels. In particular, at a throttling level of 20%, the termination of the potential core was the fastest, and the decay rate of the maximum velocity in the x-axis was the highest. These aspects resulted in the largest change in the spray angle and SMD at a throttling level of 20%. The normalized spray angle and SMD trends were obtained with the decay rate, which is related to the skip distance. Finally, the standard deviation between the throttling levels at each skip distance was analyzed. From a design point of view, it was decided to select a skip distance with a small standard deviation. Because the standard deviation of the SMD continued to increase with the skip distance, the appropriate skip distance was considered in terms of the spray angle, and it was observed that this value was approximately 0.91.

The presented findings are expected to help understand the relationship between the spray characteristics and skip distance. In addition, as the skip distance is a key parameter to be determined at the design stage of pintle injectors, the presented findings may provide guidance for the design of effective injectors to be used in reusable launch vehicles.

In the future, when spray characteristics are set for a target engine, these results will be of reference to estimate the control range for the annular flow’s orifice size. The procedures and results of this study can be applied to a linear control system for simultaneous control of the orifice sizes for radial and annular flows. Thus, an optimal throttleable pintle injector with high atomization efficiency can be realized.

REFERENCES

[1] M. J. Casiano, J. R. Hulka, V. Yang, Liquid-propellant rocket engine throttling: a comprehensive review, J. Propul. Power, 26 (5) (2010) 897-923.

[2] G. W. Elverum, R. Hills, Variable thrust bipropellant rocket engine, U.S. Patent, US3205656A, 1965.

[3] G. A. Dressler, Summary of deep throttling rocket engines with emphasis on Apollo LMDE, 42nd AIAA/ASME/SAE/ASEE Joint Propulsion Conference & Exhibit, Sacramento, CA, 2006.

[4] E. M. Betts, R. A. Frederick, A historical systems study of liquid rocket engine throttling capabilities, 46th AIAA/ASME/SAE/ASEE Joint Propulsion Conference & Exhibit, Nashville, TN, 2010.

[5] R. J. Johnson, B. R. Boyd, T. H. Smith, Application of the Mira 150A variable-thrust engine to manned lunar flying systems, J. Spacecraft Rockets, 5 (7) (1968) 849-851.

[6] Main propulsion quick reference data – Descent propulsion section.

[7] G. A., Dressler, J. M. Bauer, TRW pintle engine heritage and performance characteristics, 36th AIAA/ASME/SAE/ASEE Joint Propulsion Conference & Exhibit, Huntsville, AL, 2000.

[8] D. T. Harrje, Liquid propellant rocket combustion instability, NASA, NASA-

SP-194, 1972.

[9] C. G. Yue, J. X. Li, X. Hou, X. P. Feng, S. J. Yang, Summarization on variable liquid thrust rocket engines, Sci. China E: Technol. Sci. 52 (2009) 2918–2923.

[10] E. Seedhouse, SpaceX - making commercial spaceflight a reality, Springer, New York, 2013.

[11] J. M. Gromski, A. N. Majamaki, S. G. Chianese, V. D. Weinstock, T. S. Kim, Northrop Grumman TR202 LOX/LH2 deep throttling engine technology project status," 46th AIAA/ASME/SAE/ASEE Joint Propulsion Conference & Exhibit, Nashville, TN, 2010.

[12] B. L. Austin, S. D. Heister, W. E. Anderson, Characterization of pintle engine performance for nontoxic hypergolic bipropellants, J. Propul. Power, 21 (4) (2005) 627-635.

[13] M. J. Bedard, T. W. Feldman, A. Rettenmaier, W. Anderson, Student design/build/test of a throttleable LOX-LCH4 thrust chamber, 48th AIAA/SAE/ASEE Joint Propulsion Conference & Exhibit, Atlanta, Ga., 2012.

[14] R. N. Rezende, A. Pimenta, V. C. Perez, Experiments with pintle injector design and development," 51th AIAA/SAE/ASEE Joint Propulsion Conference, Orlando, FL, 2015.

[15] B. B. Vasques, O. J. Haidn, “Effect of pintle injector element geometry on combustion in a liquid oxygen/liquid methane rocket engine, 7th European

Conference for Aeronautics and Aerospace Sciences, Milan, Italy, 2017.

[16] S. Ninish, A. Vaidyanathan, K. Nandakumar, Spray characteristics of liquid-liquid pintle injector, Exp. Therm. Fluid Sci., 97 (2018) 324-340.

[17] K. Sakaki, H. Kakudo, S. Nakaya, M. Tsue, H. Isochi, K. Suzuki, K. Makino, T. Hiraiwa, Optical measurements of ethanol/liquid oxygen rocket engine combustor with planar pintle injector, 51th AIAA/SAE/ASEE Joint Propulsion Conference, Orlando, FL, 2015.

[18] K. Sakaki, T. Funahashi, S. Nakaya, M. Tsue, R. Kanai, K. Suzuki, T. Inagawa, T. Hiraiwa, Longitudinal combustion instability of a pintle injector for a liquid rocket engine combustor, Combust. Flame, 194 (2018) 115-127.

[19] X. Fang, C. Shen, Study on atomization and combustion characteristics of LOX/methane pintle injectors, Acta Astronaut. 136 (2017) 369-379.

[20] H. Ryu, I. Yu, T. Kim, Y. Ko, S. Kim, H. Kim, Combustion performance of the canted slit type pintle injector rocket engine by blockage factor, Proceedings of the Korean Society of Propulsion Engineers Conference, Jeju, Korea, 2016.

[21] I. Yu, S. Kim, Y. Ko, S. Kim, J. Lee, H. Kim, Combustion performance of a pintle injector rocket engine with canted slit shape by characteristic length and total momentum ratio, J. Korean Soc. Propuls. Eng., 21 (1) (2017) 36-43.

[22] S. Kim, W. Kim, T. Kim, Y. Ko, S. Kim, H. Kim, Analysis on combustion phenomena by spray pattern of canted slit type pintle injector, Proceedings of

the Korean Society of Propulsion Engineers Conference, Jeju, Korea, 2016.

[23] M. Son, K. Yu, J. Koo, O. C. Kwon, J. S. Kim, Injection condition effects of a pintle injector for liquid rocket engines on atomization performances, J. ILASS-Korea, 20 (2) (2015) 114-120.

[24] M. Son, K. Radhakrishnan, Y. Yoon, J. Koo, Numerical study on the combustion characteristics of a fuel-centered pintle injector for methane rocket engines, Acta Astronaut. 135 (2017) 139-149.

[25] K. Radhakrishnan, M. Son, K. Lee, J. Koo, Lagrangian approach to axisymmetric spray simulation of pintle injector for liquid rocket engines," Atomization Spray., 28 (5) (2018) 443-458.

[26] K. Sakaki, H. Kakudo, S. Nakaya, M. Tsue, Combustion characteristics of ethanol/liquid-oxygen rocket-engine combustor with planar pintle injector, J. Propul. Power, 33 (2017) 514–521.

[27] S. Gordon, B. J. McBride, Computer program for calculation of complex chemical equilibrium compositions and applications II. users manual and program description, NASA Reference Publication 1311, E-8017-1, 1996.

[28] S. D. Heister, Handbook of Atomization and Sprays, Springer, New York, 2011.

[29] S. Lee, J. Koo, Y. Yoon, Technology and developing trends of pintle injector for throttleable engine, J. Kor. Soc. Propuls. Eng., 21 (4) (2017) 107-118.

[30] K. Yu, M. Son, J. Koo, Effects of opening distance on liquid-gas spray of pintle

injector under atmospheric condition, J. Korean Soc. Aeronaut. Space Sci., 4. (7) (2015) 585-592.

[31] H. Kim, H. Lee, P. Park, S. Yang, Spray characteristics of liquid-liquid pintle injectors, Proc. Kor. Soc. Propul. Eng. Conf., Gangwon-do, Korea, 2014.

[32] I. Yu, T. Kim, H. Ryu, Y. Ko, S. Kim, P. Park, Combustion performance of a pintle injector rocket engine with rectangular slot shapes, Proc. Kor. Soc. Propul. Eng. Conf. Gyeongju, Korea, 2015.

[33] V. Yang, M. Habiballah, J. Hulka, M. Popp, Liquid rocket thrust chambers: aspects of modeling, analysis, and design, Prog Astronaut. Aeronaut. 200 (2004) 157–162.

[34] A. H. Lefebvre, Atomization and sprays, Hemisphere Publishing Corporation, New York, 1989.

[35] Y. Yoon, H. Koh, D. Kim, T. Khil, Spray visualization using laser diagnostics, J. Korean Society of Visualization, 3 (2) (2005) 3-13.

[36] A. K. Prasad, K. Jensen, Scheimpflug stereocamera for particle image velocimetry in liquid flows, Applied Optics, 34 (30) (1995) 7092-7099.

[37] M. Storch, Y. N. Mishra, M. Koegl, E. Kristensson, S. Will, L. Zigan, E. Berrocal, Two-phase SLIPI for instantaneous LIF and Mie imaging of transient fuel sprays, Optics Letters, 41 (23) (2016) 5422-5425.

[38] R. Abu-Gharbieh, J. L. Persson, M. Försth, A. Rosén, A. Karlström, T.

Gustavsson, Compensation method for attenuated planar laser images of optically dense sprays, Appl. Optics, 39 (8) (2000) 1260-1267.

[39] R. W. Tate, Spray patternation, J. Ind. Eng. Chem., 52 (10) (1960) 49A-58A.

[40] Y. Cao, The image analysis for optical Spray patternation, M.S. Thesis, Queen’s University, 2000.

[41] Х. В. Кесаев, Расчёт форсунок двигателя В.Д.Курпатенков, Publishing House MAI, Moscow, 1987.

[42] S. Lee, D. Kim, J. Koo, Y. Yoon, Spray characteristics of a pintle injector based on annular orifice area, Acta Astronaut. 167 (2020) 201–211.

[43] S. Lee, D. Kim, J. Koo, Y. Yoon, Corrigendum to “Spray characteristics of a pintle injector based on annular orifice area” [Acta Astronautica 167 (2020) 201-211], Acta Astronaut. 173 (2020) 473–474.

[44] C. Yun, J. Tucker, K. Travis, T. Dib, T. Rice, B. Viggiano, Liquid fuel rocket engine capstone, Portland state university, Final report, Portland, Oregon, 2016.

[45] P. Cheng, Q. Li, S. Xu, Z. Kang, On the prediction of spray angle of liquid-liquid pintle injectors, Acta Astronaut. 138 (2017) 145–151.

[46] I. Lopez, Design of a 2000 lbf LOX/LCH4 throttleable rocket engine for a vertical lander, Dissertation, The University of Texas at El Paso, 2017.

[47] H. Chen, Q. Li, P. Cheng, Experimental research on the spray characteristics of pintle injector, Acta Astronaut. 162 (2019) 424–435.

[48] H. Kim, H. Kang, S. Kwon, A feasibility study of using pintle injector as sole-throttling device for shallow throttling condition, Acta Astronaut. 167 (2020) 272–279.

[49] M. Son, K. Radhakrishnan, J. Koo, O. C. Kwon, H. D. Kim, Design procedure of a movable pintle injector for liquid rocket engines, J. Propul. Power, 33 (2017) 858–869.

[50] K. Radhakrishnan, M. Son, K. Lee, J. Koo, Effect of injection conditions on mixing performance of pintle injector for liquid rocket engines, Acta Astronaut. 150 (2018) 105–116.

[51] K. Lee, D. Shin, M. Son, H. Moon, J. Koo, Flow visualization of cryogenic spray from a movable pintle injector, J. Vis. 22 (2019) 773–781.

[52] Y. Chang, J. Zou, Q. Li, P. Cheng, K. Zhou, Numerical study on combustion and heat transfer of a GOX/GCH4 pintle injector, Proc. 2018 Asia-Pacific Int. Symp. Aerosp. Technol. Chengdu, China, 2018.

[53] S. Huang, Y. Li, J. Zhou, S. Liu, H. Peng, Effects of the pintle injector on H_2/air continuous rotating detonation wave in a hollow chamber, Int. J. Hydrog. Eng. 44 (2019) 14044–14054.

[54] S. Huang, J. Zhou, S. Liu, H. Peng, Effects of pintle injector on ethylene-air rocket-based continuous rotating detonation, Acta Astronaut. 164 (2019) 311–320.

[55] E. Sekula, J. M. Redondo, The structure of turbulent jets, vortices and boundary layer: laboratory and field observations, Il Nuovo Cimento, 31 (2008) 893–907.

[56] P. Deogonda, V. N. Chalwa, M. C. Murugesh, V. Dixit, Wall static pressure distribution due to confined impinging circular air jet, Int. J. Res. Eng. Technol. 3 (2014) 591–597.

[57] S. Ashforth-Frost, K. Jambunathan, C. F. Whitney, S. J. Ball, Heat transfer from a flat plate to a turbulent axisymmetric impinging jet, Proc. Inst. Mech. Eng. 211 (1997) 167–172.

[58] A. Verhoff, The tow-dimensional, turbulent wall jet with and without an external free stream, Report, 626 Dept. of Aeronautical Engineering, Princeton Univ., Princeton, NJ, 1963.

[59] J. Yushu, X. Xu, Q. Yang, S. Zhu, Numerical investigation of flame appearance and heat flux and in a deep-throttling variable thrust rocket engine, Aerosp. Sci. Technol. 88 (2019) 457-467.

초 록

민간 주도의 우주 발사체 시장 성장과 함께 초소형 위성 시장이 커짐에 따라 상업 발사 서비스 시장 경쟁이 치열해지면서 발사 비용을 낮추기 위한 차세대 발사체 개발이 활발히 이루어지고 있다. 재사용 발사체는 저비용 발사 임무를 실현하기 위한 중요 기술로, 지상 또는 해상 착륙 시 엔진 회수를 위한 소프트 랜딩 기술이 매우 중요하게 여겨진다. 소프트 랜딩은 발사체 엔진의 추력을 조절함으로써 실현 가능하며, 이를 위한 몇 가지 기술들 중 추진제 오리피스 면적 제어를 이용한 방식이 신뢰성 있다고 여겨지고 있다.

핀틀 분사기는 면적 조절을 통한 추력 제어 방식의 대표적 시스템이다. 미국 TRW 사에 의해 고안된 후, 2000년대 초반부터 국내외에서 핀틀 분사기에 대한 개발 및 연구가 수행되고 있으나, 공개된 문헌 및 정보가 한정적이며 제한적이기 때문에 설계에 있어 여전히 어려움이 존재한다. 특히, 핀틀 분사기는 성능에 영향을 미치는 여러 형상 변수들을 가지기 때문에 이에 대한 연구가 필수적이다.

따라서 본 연구에서는 중요 형상 변수들과 분무 특성과의 관계를 살펴보았다. 핀틀 분사기의 분무 특성은 연소 성능과 밀접하게 관련되어 있기 때문에 수류 실험을 통해 이를 분석하고자 하였다. 먼저, 핀틀 분사기의 최적 설계를 위한 데이터베이스 마련을 위해 5:1의 추력비를 가지는 소형 액체로켓엔진용 핀틀 분사기에 대해 유체를 고르게 분무하기 위한 내부 유로 설계를 수행하였다. 추력이 변하는 동안 구동 장치의 축 방향 동심도를 유지하기 위해 다양한 형상 케이스를 고안하였고 수치해석 및 실험을 통해 최적 형상 조건을 모색하였다.

이후 annular flow의 오리피스 면적 조절과 관련된 인자인 gap distance (G)를 바꿔가며 분무 특성에 미치는 영향을 살펴보았다. 실험 결과, 동일 추력 레벨에서 G가 감소할 경우, annular flow의 운동량이 상대

적으로 커지기 때문에 분무각은 감소하였다. G가 고정되어 있을 경우에는 추력 레벨이 변하더라고 분무각은 거의 일정하였다. 액적 직경의 경우도 G가 감소함에 따라 작아지는 경향을 보였다. SMD와 분열과 관련된 무차원수인 We 및 J와의 관계를 살펴본 결과, 핀틀 분사기가 크게 두 가지 미립화 과정을 가지는 것을 알 수 있었다. 초기 핀틀 끝 단에서 radial flow와 annular flow가 수직 충돌 시 두 유체의 운동량 차로 인한 액막 분열과 함께 두 유체 표면에서의 전단력으로 인한 추가 분열이 진행되는 것으로 분석되었다. 분무각 및 SMD에 대한 실험식을 구하였고, 이를 통해 전 추력 구간에서 특정 SMD를 유지하기 위한 G의 제어 범위를 도출하였다.

핀틀 분사기의 또 다른 중요 형상 변수인 skip distance에 대해서도 수류 실험을 수행하였고, skip distance의 증가에 따라 분무각 및 SMD가 비례 관계를 가지는 것을 확인하였다. Annular flow가 핀틀 표면을 따라 이동하면서 마찰 및 대기와의 상호작용으로 인해 유속이 감소하게 되고 이에 따른 운동량 손실률 증가 등으로 인해 이러한 경향이 나타났다. Skip distance에 따른 분무 특성 변화율은 저 추력 조건으로 갈수록 커졌고, 특히 20% 조건에서 가장 큰 폭을 보였다. 이러한 경향성을 좀 더 자세히 분석하기 위해 핀틀 표면 부근에서 annular flow의 축 방향 속도 분포를 수치적으로 분석하였다. 전 추력 조건에서 오리피스 출구 시작점으로부터 일정 거리까지 속도가 일정하게 유지되는 potential core와 속도 프로파일이 유사성을 가지는 developed region이 관찰되었다. 특히, 20% 추력 조건에서 potential core 영역이 가장 짧았고 최대 속도 감소율도 가장 높은 것으로 나타났다. 이로 인해 20% 추력 조건에서 분무각과 SMD가 가장 크게 변화된 것으로 보였다. Skip distance에 따른 속도 감소율을 통해 분무각 및 SMD 변화율을 얻었고, 마지막으로 설계 관점에서 각 추력 레벨간의 표준 편차를 고려하여 적절한 skip distance가 제안되었다.

본 연구를 통해 핀틀 분사기 설계 단계에서 고려돼야 할 주요 형상 변수들에 대한 자료를 확보하였다. 이러한 결과는 skip distance와 분무 특

성과의 관계를 이해하는데 도움이 될 것으로 기대된다. 또한, annular flow의 오리피스 면적 제어 범위 설정을 위한 참고 자료로서 분무 성능 향상을 위한 추력 제어 시스템 설계에 활용 가능하다. 향후 가변추력용 엔진을 위한 효과적인 분사기 설계에 대한 기초자료로서 이용될 것으로 기대된다.

중심어: 핀틀 분사기, 추력 제어, 형상 변수, 분무 특성, 축 방향 오리피스 면적, 갭 거리, 스킵 거리

학 번: 2016-30188